# Estimating Spatially-Smoothed Fiber Orientation Distribution

Jilei Yang \*
Department of Statistics, University of California, Davis and Jie Peng<sup>†</sup>
Department of Statistics, University of California, Davis

#### Abstract

Diffusion-weighted magnetic resonance imaging (D-MRI) is an in-vivo and non-invasive imaging technology to probe anatomical architectures of biological samples. The anatomy of white matter fiber tracts in the brain can be revealed to help understanding of the connectivity patterns among different brain regions. In this paper, we propose a novel  $Nearest-neighbor\ Adaptive\ Regression\ Model\ (NARM)$  for adaptive estimation of the fiber orientation distribution (FOD) function based on D-MRI data, where spatial homogeneity is used to improve FOD estimation by incorporating neighborhood information. Specifically, we formulate the FOD estimation problem as a weighted linear regression problem, where the weights are chosen to account for spatial proximity and potential heterogeneity due to different fiber configurations. The weights are adaptively updated and a stopping rule based on nearest neighbor distance is designed to prevent over-smoothing. NARM is further extended to accommodate D-MRI data with multiple b-values.

Comprehensive simulation results demonstrate that NARM leads to satisfactory FOD reconstructions and performs better than voxel-wise estimation as well as competing smoothing methods. By applying NARM to real 3T D-MRI datasets, we demonstrate the effectiveness of NARM in recovering more realistic crossing fiber patterns and producing more coherent fiber tracking results, establishing the practical value of NARM for analyzing D-MRI data and providing reliable information on brain structural connectivity.

Keywords: propagation-separation method, minimum nearest-neighbor distance, HCP

<sup>\*</sup>The authors gratefully acknowledge the following support: UCD Dissertation Year Fellowship (JLY), NIH 1R01EB021707 (JLY and JP), NSF-DMS-1148643 (JP) and NSF-DMS-1915894 (JP).

<sup>&</sup>lt;sup>†</sup>Correspondence author: jiepeng@ucdavis.edu

## 1 Introduction

The study of the brain structure and how it functions is an old yet essential topic. As an in-vivo, non-invasive and no-radiation-included medical imaging technology, Diffusion-weighted MRI (D-MRI) has become widely used by neuro-scientists to probe architecture of biological tissues. The detailed anatomy of white matter fiber tracts in the brain can be revealed by making use of diffusion displacement measures of water molecules in D-MRI, since in white matter, water usually diffuses faster along the fiber bundles which makes the water diffusion anisotropic. Reconstructing white matter fiber tracts is of great value in understanding the brain structure and its functionality (Mori 2007, Sporns 2010). One of the earliest D-MRI technology is the well-known diffusion tensor imaging (DTI) (Basser et al. 1994). Recently, high angular resolution diffusion imaging (HARDI) has become of great interest in accurate extraction of fiber tracts information, e.g., the orientation of intra-voxel crossing fibers, through diffusion measurements along a large number of gradient directions (Tuch et al. 2002). The white matter fiber tracts can then be reconstructed by applying tracking algorithms (tractography) (Basser et al. 2000, Wong et al. 2016).

There are many models developed for HARDI data, including angular reconstruction models such as fiber orientation distribution (FOD) (Tournier et al. 2004, 2007) and diffusion orientation distribution function (ODF) (Tuch 2004, Descoteaux et al. 2007, 2009). In this paper, we focus on one particular model: the FOD, which is designed to describe the angular dependence of the axonal fiber bundles by making use of sharp geometric features (Jensen et al. 2016). White matter fiber reconstruction through tractography can greatly benefit from a good estimation of the FOD.

One commonly used method in FOD estimation is based on the spherical deconvolution framework described in Tournier et al. (2004, 2007), where the key to its success is a parsimonious representation of the FOD in a suitable basis. Early studies of the FOD estimation are mostly based on spherical harmonics (SH) representations of the FOD (Tournier et al. 2004, 2007). However, due to the global support of the SH basis functions, they do not represent the FOD efficiently when spiky features exist, which is usually the case in well-defined fiber tracts. Recently, Yan et al. (2018) has proposed a new FOD estimation method called SN-lasso based on spherical needlets (SN) representations of the FOD. As

smooth spherical functions localized in both space and frequency, spherical needlets form a tight spherical frame and thus provide parsimonious and stable representations for spherical functions with localized sharp peaks such as the FOD (Narcowich et al. 2006b,a). By introducing spherical needlets, the FOD estimation problem is reformulated as a linear regression problem where the needlet coefficients of the FOD are the variables to estimate. An  $l_1$  penalty is imposed on these needlet coefficients to ensure the sparse representation. Moreover, a nonnegative constraint on the estimated FOD is also imposed to guarantee the nonnegativeness of the probability density function FOD. In this paper, we focus on the SN-lasso method in FOD estimation, since it would lead to more accurate and stable reconstruction results of the FOD and preserve its sharp features.

Most of the existing methods for fiber reconstruction, including the FOD estimation method SN-lasso, are developed in each voxel and perform voxel-wise fiber reconstruction independently. However, the spatial constraint, which is the structural nature of the HARDI data, is essentially ignored by these methods. Following Rao et al. (2016), the direction of single fiber bundles are expected to change smoothly along the dominant fiber direction from one voxel to its neighborhood voxels, until it reaches the boundaries between fiber tracts. Similarly, the directions of crossing fiber bundles are expected to vary smoothly along their own dominant fiber directions from one voxel to its surrounding voxels in the fiber crossing region.

Until recently, a few methods have been proposed for fiber reconstruction where spatial constraint is incorporated for potential improvement. Some of these methods are based on the well-known propagation-separation method (Polzehl & Spokoiny 2000, 2006), which is developed specifically for model functions with large homogeneous regions and sharp discontinuities. Although the original propagation-separation method is only applicable in denoising the usual images, several extensions of this method are developed in the area of fiber reconstruction. For example, smoothing and estimation on DTI data via an anisotropic structural adaptive smoothing procedure (Tabelow et al. 2008), smoothing raw HARDI images based on structural adaptive smoothing in both voxel space and diffusion-gradient space (Becker et al. 2012, 2014), spatial and adaptive analysis of neuroimaging data using a multiscale adaptive regression model (MARM) which integrates propagation-

separation method with voxel-wise statistical modeling (Li et al. 2011), spatial and adaptive estimation of ODF using a penalized multiscale adaptive regression model (PMARM) which integrates MARM, propagation-separation method and Lasso (Rao et al. 2016). Other spatial smoothing methods using strategies different from propagation-separation method include spatial smoothing and estimation of DTI (Liu et al. 2013, Yu & Li 2013), spatial smoothing of HARDI with Bayesian spatial regularization (Raj et al. 2011), spatial smoothing of estimated diffusion directions via clustering (Wong et al. 2016) and so on.

In this paper, we propose a novel Nearest-neighbor Adaptive Regression Model (NARM) to conduct spatially smoothed and locally adaptive estimation of FODs across all voxels. NARM can be regarded as a natural integration of the extended propagation-separation method and the voxel-wise FOD estimation method SN-lasso. Specifically, for the FOD estimation in each voxel, instead of optimizing a single likelihood function based on the voxel itself (i.e., the linear regression model in SN-lasso), we incorporate its neighborhood information by optimizing the sum of weighted likelihood functions based on the voxel and its neighborhood voxels. The weights are chosen appropriately to account for spatial proximity and potential heterogeneity due to different fiber configurations, measured by both the spatial distance between voxels and the similarity between FOD estimates.

Similar to the PMARM method proposed by Rao et al. (2016), we adaptively update these weights and also use a stopping rule to avoid over-smoothing. However, NARM differs from PMARM in three major aspects. First, we use Hellinger distance in measuring similarity between FODs, where Hellinger distance is proposed specifically for probability distribution function and is more sensitive to peak value difference. In contrast, the PMARM method uses the  $l_2$  distance in FOD similarity measurement. Second, we use a simple yet effective stopping rule based on the minimum distance between the voxel and its nearest neighbors, whereas the PMARM method relies on a more complicated stopping rule with hyper-parameters not easy to tune in practice. Third, we implement weight-rescaling for voxels which are either extremely easy or extremely hard to be smoothed, to avoid potential over-smoothing or under-smoothing issues. On the contrary, the PMARM method does not cover this. In addition to the extension of the propagation-separation method, we also extend the SN-lasso to the cases where diffusion measurements are sampled with

multiple b-values. This is actually the format of D-MRI dataset in the WU-Minn Human Connectome Project database (Van Essen et al. 2013).

We conduct extensive simulation studies based on two-dimensional and three-dimensional regions of synthetic data to demonstrate the effectiveness of our proposed NARM method, and to make comparisons with the voxel-wise SN-lasso method and the PMARM method. We also show the advantages of FOD estimation based on multiple b-values over FOD estimation based on single b-value. Moreover, we implement NARM to one real 3-T D-MRI dataset of healthy individual from the WU-Minn Human Connectome Project database (Van Essen et al. 2013). The tractography results based on the estimated FODs from our proposed method tend to show more clear patterns of fiber tracts with less noise, compared to the estimated FODs from voxel-wise method.

The rest of paper is organized as follows. Section 2 formally defines the problem and introduces the voxel-wise FOD estimation method SN-lasso. Section 3 proposes the *Nearest-neighbor Adaptive Regression Model* (NARM) in detail. Section 4 and 5 present the experimental results on synthetic and real datasets respectively. Section 6 concludes our work and discusses future directions. Technical details can be found in an Appendix. Additional details are deferred to a Supplementary Material.

## 2 Voxel-wise FOD estimation

# 2.1 Spherical convolution model

We estimate the FOD function  $F(\boldsymbol{v},\cdot)$  for each voxel  $\boldsymbol{v}$  based on the observed diffusion weighted measurements  $\boldsymbol{y}(\boldsymbol{v}) = \{y_i(\boldsymbol{v})\}_{i=1}^n$  corresponding to n gradient directions. These diffusion weighted measurements can be regarded as the noise corrupted evaluations of the diffusion signal function  $S(\boldsymbol{v},\cdot)$  at these n gradient directions. Thus, it is crucial to understand the relationship between the FOD  $F(\boldsymbol{v},\cdot)$  and the diffusion signal function  $S(\boldsymbol{v},\cdot)$ . Following Tournier et al. (2004, 2007), the diffusion signal function  $S(\boldsymbol{v},\cdot)$  can be represented by the spherical convolution of the FOD function  $F(\boldsymbol{v},\cdot)$ :  $\mathbb{S}^2 \to \mathbb{R}^+$ , a symmetric spherical probability density function, and the response function  $R(\cdot)$ :  $L^1([-1,1]) \to \mathbb{R}$ , an azimuthal symmetric kernel function which represents the diffusion signal along a single

fiber bundle and is assumed to be the same across voxels. Hereafter we assume the response function  $R(\cdot)$  is known. In practice,  $R(\cdot)$  can be estimated by applying tensor models onto voxels with a single dominant fiber bundle.

The formal definition of the spherical convolution model at voxel v follows:

$$S(\boldsymbol{v}, \boldsymbol{x}) = R * F(\boldsymbol{v}, \boldsymbol{x}) = \int_{\mathbb{S}^2} R(\boldsymbol{x}^T \boldsymbol{y}) F(\boldsymbol{v}, \boldsymbol{y}) d\omega(\boldsymbol{y}), \qquad \boldsymbol{x} \in \mathbb{S}^2.$$
 (1)

Following Descoteaux et al. (2007), Yan et al. (2018), the real symmetric spherical harmonic (SH) functions  $\{\Phi_{lm}: m=-l,\ldots,l\}_{l=0,2,4,\ldots}$  form an orthonormal basis for the square integrable real symmetric functions on  $\mathbb{S}^2$ . By the orthonormality of the real symmetric SH basis, the diffusion signal function  $S(\boldsymbol{v},\boldsymbol{x})$  can be expressed as:

$$S(\boldsymbol{v}, \boldsymbol{x}) = \sum_{l} \sum_{m=-l}^{l} s_{lm} \Phi_{lm}(\boldsymbol{x}) = \sum_{l} \sqrt{\frac{4\pi}{2l+1}} r_{l} \sum_{m=-l}^{l} f_{lm} \Phi_{lm}(\boldsymbol{x}),$$

where  $s_{lm} := \langle S, \Phi_{lm} \rangle$ ,  $r_l := \langle R, \Phi_{l0} \rangle$  and  $f_{lm} := \langle F, \Phi_{lm} \rangle$  are the spherical harmonic coefficients of the diffusion signal function, response function and FOD respectively.

Now we assume the real symmetric SH basis up to level  $l_{\text{max}}$  can well approximate the diffusion signal function, response function and FOD. The observed diffusion weighted measurements y(v) can then be modeled as:

$$y(v) = \Phi R f(v) + \epsilon, \tag{2}$$

where  $\Phi$  is an  $n \times L$  matrix  $(L = (l_{\text{max}} + 1)(l_{\text{max}} + 2)/2$  is the number of basis functions) consisting of L SH function evaluations at n gradient directions;  $\mathbf{R}$  is an  $L \times L$  diagonal matrix with diagonal elements  $\sqrt{\frac{4\pi}{2l+1}}r_l$  in blocks of length 2l+1;  $\mathbf{f}(\mathbf{v})$  is an  $L \times 1$  vector of FOD's SH coefficients to be estimated; and  $\boldsymbol{\epsilon}$  is an  $n \times 1$  error vector.

#### 2.2 SN-lasso method

In SN-lasso, we represent the FOD by symmetric spherical needlets (SN) basis. The real symmetric SN functions form a tight frame for the square integrable real symmetric functions on S<sup>2</sup>, and they are localized in both scale and space. Thus, the FOD can be well approximated by a small set of SN functions since most of the FODs are either constant or with a few localized sharp peaks.

Now we set the maximum level of SN basis  $j_{\text{max}} = \lceil \log_2(l_{\text{max}}) \rceil$  and N being the corresponding number of SN basis functions.  $j_{\text{max}}$  is selected such that the first N SN functions can linearly represent the SH functions up to level  $l_{\text{max}}$ . In this case, the SH coefficient vector  $\mathbf{f}(\mathbf{v})$  in (2) can be further expressed as  $\mathbf{C}\boldsymbol{\beta}(\mathbf{v})$ , where  $\mathbf{C}$  is an  $L \times N$  transition matrix and can be pre-computed (Narcowich et al. 2006 a, Yan et al. 2018), and  $\boldsymbol{\beta}(\mathbf{v})$  is an  $N \times 1$  vector of FOD's SN coefficients. (2) can then be rewritten accordingly:

$$y(v) = \Phi RC\beta(v) + \epsilon. \tag{3}$$

Based on the sparsity nature of the FOD's SN coefficients  $\beta(v)$ , SN-lasso proposes to estimate  $\beta(v)$  by an  $l_1$ -penalized linear regression model:

$$\hat{\boldsymbol{\beta}}(\boldsymbol{v}) = \arg \min_{\boldsymbol{\beta}(\boldsymbol{v}): \tilde{\boldsymbol{\Phi}}\boldsymbol{C}\boldsymbol{\beta}(\boldsymbol{v}) \succeq \boldsymbol{0}} \frac{1}{2} ||\boldsymbol{y}(\boldsymbol{v}) - \boldsymbol{\Phi}\boldsymbol{R}\boldsymbol{C}\boldsymbol{\beta}(\boldsymbol{v})||_{2}^{2} + \lambda ||\boldsymbol{\beta}(\boldsymbol{v})||_{1}.$$
(4)

Here  $\lambda || \boldsymbol{\beta}(\boldsymbol{v}) ||_1$  is the lasso regularizer with tuning parameter  $\lambda \geq 0$ , which leads to sparse representation of  $\boldsymbol{\beta}(\boldsymbol{v})$ .  $\tilde{\boldsymbol{\Phi}}$  is the matrix of L SH functions evaluated on a dense spherical grid, and  $\tilde{\boldsymbol{\Phi}}\boldsymbol{C}\boldsymbol{\beta}(\boldsymbol{v}) \succeq \boldsymbol{0}$  guarantees that the estimated FOD on this dense grid is nonnegative. Notice both the design matrix  $\boldsymbol{\Phi}\boldsymbol{R}\boldsymbol{C}$  and the constraint matrix  $\tilde{\boldsymbol{\Phi}}\boldsymbol{C}$  are the same across all the voxels and can be computed in advance.

A computationally efficient algorithm based on ADMM (Alternating Directions Method of Multipliers) (Boyd et al. 2011) is developed for the optimization problem in (4), where the algorithm details are given in Appendix 7.1. A peak detection algorithm is also proposed to efficiently identify the major fiber directions according to the FOD estimation, where more details are given in Yan et al. (2018).

# 3 Spatially-smoothed FOD estimation

The FOD estimation method SN-lasso is a voxel-wise method which is implemented for each voxel independently by using only the D-MRI information from the voxel itself. However, the spatial smoothness nature of HARDI data across voxels is essentially ignored by this method. For example, for single fiber bundle in a voxel, its direction is expected to vary smoothly along the major fiber direction from the voxel to its neighborhood, except at the boundaries between fiber tracts. For crossing fiber bundles in a voxel, their directions

are also expected to smoothly follow their own major fiber directions respectively from the voxel to its surrounding voxels. The spatial constraint in HARDI data is indeed very important and worthy exploring to further improve the reconstruction of fiber tracts.

To take the spatial constraint into consideration, we propose a new spatial smoothing method in FOD estimation, named Nearest-neighbor Adaptive Regression Model (NARM). The fundamental idea is the implementation of local likelihood modeling (Fan & Gijbels 1996), that is, instead of optimizing a single likelihood function at voxel  $\boldsymbol{v}$  based on the observed diffusion measurements  $\boldsymbol{y}(\boldsymbol{v})$  only from voxel  $\boldsymbol{v}$  itself (i.e., Eq. (4) up to a constant), we incorporate signals from its neighborhood voxels as well and optimize the sum of weighted likelihood functions within a neighborhood centered at voxel  $\boldsymbol{v}$ . Here without loss of generality, we assume all the voxels are located in the Cartesian grid with unit distance between adjacent voxels. Let  $N_d(\boldsymbol{v}) := \{\boldsymbol{v}': ||\boldsymbol{v}-\boldsymbol{v}'||_2 \leq d\}$  denote a (spherical) neighborhood with radius d centered at voxel  $\boldsymbol{v}$ , and  $\omega_d(\boldsymbol{v}, \boldsymbol{v}')$  denote a weight function of pair  $(\boldsymbol{v}, \boldsymbol{v}')$  such that  $\sum_{\boldsymbol{v}' \in N_d(\boldsymbol{v})} \omega_d(\boldsymbol{v}, \boldsymbol{v}') = 1$  and  $\omega_d(\boldsymbol{v}, \boldsymbol{v}') \geq 0$ . The FOD's SN coefficients  $\boldsymbol{\beta}_d(\boldsymbol{v})$  corresponding to neighborhood  $N_d(\boldsymbol{v})$  can then be estimated from the  $l_1$ -penalized weighted linear regression model:

$$\hat{\boldsymbol{\beta}}_{d}(\boldsymbol{v}) = \arg \min_{\boldsymbol{\beta}(\boldsymbol{v}): \tilde{\boldsymbol{\Phi}}\boldsymbol{C}\boldsymbol{\beta}(\boldsymbol{v}) \succ \mathbf{0}} \sum_{\boldsymbol{v}' \in N_{d}(\boldsymbol{v})} \omega_{d}(\boldsymbol{v}, \boldsymbol{v}') \cdot \frac{1}{2} ||\boldsymbol{y}(\boldsymbol{v}') - \boldsymbol{\Phi}\boldsymbol{R}\boldsymbol{C}\boldsymbol{\beta}(\boldsymbol{v})||_{2}^{2} + \lambda ||\boldsymbol{\beta}(\boldsymbol{v})||_{1}$$

$$= \arg \min_{\boldsymbol{\beta}(\boldsymbol{v}): \tilde{\boldsymbol{\Phi}}\boldsymbol{C}\boldsymbol{\beta}(\boldsymbol{v}) \succ \mathbf{0}} \frac{1}{2} ||\boldsymbol{y}_{d}(\boldsymbol{v}) - \boldsymbol{\Phi}\boldsymbol{R}\boldsymbol{C}\boldsymbol{\beta}(\boldsymbol{v})||_{2}^{2} + \lambda ||\boldsymbol{\beta}(\boldsymbol{v})||_{1},$$
(5)

where  $\mathbf{y}_d(\mathbf{v}) = \sum_{\mathbf{v}' \in N_d(\mathbf{v})} \omega_d(\mathbf{v}, \mathbf{v}') \mathbf{y}(\mathbf{v}')$  is the weighted average of observed diffusion measurements within the neighborhood  $N_d(\mathbf{v})$ . Note that when d is set to be 0, the neighborhood  $N_d(\mathbf{v})$  contains only one voxel  $\mathbf{v}$ , and Eq. (5) actually coincides with Eq. (4) in the voxel-wise method SN-lasso. Following Yan et al. (2018), we select the largest value of tuning parameter  $\lambda$  in  $l_1$  penalty such that the residual sum of squares will not be significantly improved if the value of  $\lambda$  is further decreased (See Appendix 7.2 for more details).

One popular approach in local likelihood modeling is the propagation-separation method (Polzehl & Spokoiny 2000, 2006), which aims to figure out a maximal local neighborhood of each sample point where the local homogeneity assumption of parameter is justified. Inspired by the propagation-separation method, we adaptively determine the weight  $\omega_d(\mathbf{v}, \mathbf{v}')$ 

and estimate the FOD's SN coefficients  $\beta_d(\boldsymbol{v})$  across all voxels. For each voxel  $\boldsymbol{v}$ , we construct a sequence of nested (spherical) neighborhoods with increasing radii  $0 = d_0 < d_1 < \cdots < d_S$ . At  $d_0 = 0$ , the estimated coefficients  $\hat{\boldsymbol{\beta}}_{d_0}(\boldsymbol{v})$  are exactly  $\hat{\boldsymbol{\beta}}(\boldsymbol{v})$  estimated voxelwisely by Eq. (4). At the sth step, the weights  $\omega_{d_s}(\boldsymbol{v}, \boldsymbol{v}')$  are calculated by the method as detailed in the following sections where the information of the previously estimated coefficients  $\hat{\boldsymbol{\beta}}_{d_s-1}(\boldsymbol{v})$  is included, and the current estimated coefficients  $\hat{\boldsymbol{\beta}}_{d_s}(\boldsymbol{v})$  can be directly obtained afterwards. In practice, we set the series of  $d_s$  as  $d_0 = 0$ ,  $d_s = r^s$ ,  $s = 1, \dots, S$ , where the default choice of r is 1.15 and the default choice of S is 10 in two-dimensional region and 6 in three-dimensional region. The intuition of different choices of S is that we make the numbers of voxels within the largest neighborhood  $N_{d_S}(\boldsymbol{v})$  in two-dimensional region and three-dimensional region similar.

## 3.1 Weight selection

The selection of the weights  $\omega_d(\mathbf{v}, \mathbf{v}')$ ,  $\mathbf{v}' \in N_d(\mathbf{v})$  is crucial in finding a good estimation of FOD and hence a reasonable reconstruction of fiber tracts. Ideally, the weights should reflect the spatial distance between voxels, assuming that the closer the voxels are, the more useful signal information they can borrow from each other. Moreover, the weights are also expected to provide a similarity measure between the underlying true fiber directions in voxels. That is, the weight should be large if the fiber directions between two voxels are similar, so that the truly useful information can be provided by one voxel to the other; on the other hand, if the true fiber directions between two voxels are very different, the weight should be decreased to prevent incorporating spurious signals which leads to bad estimations. However, these true fiber directions are never known to us, and a natural idea is to use the estimated FODs to help determine these weights.

Let  $\mathrm{Dist}_s(\boldsymbol{v}, \boldsymbol{v}')$  denote the similarity measure between the estimated FODs in voxels  $\boldsymbol{v}$  and  $\boldsymbol{v}'$  at step s. The formula for calculating the weights  $\omega_{d_s}(\boldsymbol{v}, \boldsymbol{v}')$  is written as

$$\omega_{d_s}(\boldsymbol{v}, \boldsymbol{v}') := \frac{K_{\text{loc}}(||\boldsymbol{v} - \boldsymbol{v}'||_2/d_s)K_{\text{sim}}(\text{Dist}_s(\boldsymbol{v}, \boldsymbol{v}'))}{\sum_{\boldsymbol{v}' \in N_{d_s}(\boldsymbol{v})} K_{\text{loc}}(||\boldsymbol{v} - \boldsymbol{v}'||_2/d_s)K_{\text{sim}}(\text{Dist}_s(\boldsymbol{v}, \boldsymbol{v}'))},$$

where  $K_{\text{loc}}(\cdot)$  and  $K_{\text{sim}}(\cdot)$  are two nonnegative kernel functions.

The weight  $\omega_{d_s}(\boldsymbol{v}, \boldsymbol{v}')$  can be regarded as the combination of two independent weights: the location weight  $\omega_{\text{loc},d_s}(\boldsymbol{v},\boldsymbol{v}') := K_{\text{loc}}(||\boldsymbol{v}-\boldsymbol{v}'||_2/d_s)$  and the similarity weight  $\omega_{\text{sim},d_s}(\boldsymbol{v},\boldsymbol{v}') :=$   $K_{\text{sim}}(\text{Dist}_s(\boldsymbol{v}, \boldsymbol{v}'))$ . In NARM, we choose  $K_{\text{loc}}(u) = (1 - u^2)_+$  which only considers the voxels within the neighborhood  $N_{d_s}(\boldsymbol{v})$ . Moreover, it gives more weight to the voxel  $\boldsymbol{v}'$  closer to the voxel  $\boldsymbol{v}$ , indicating that the voxel  $\boldsymbol{v}'$  would probably contain more useful information to help FOD estimation in the voxel  $\boldsymbol{v}$ . We also choose  $K_{\text{sim}}(u) = \exp(-\gamma u^2)$  which takes small value if the estimated FODs in the voxel  $\boldsymbol{v}'$  and  $\boldsymbol{v}$  differ significantly.  $\gamma$  is a positive scalar which gives less weight to  $\boldsymbol{v}'$  on  $\boldsymbol{v}$  when it increases.

We set the similarity measure at step s,  $\mathrm{Dist}_s(\boldsymbol{v}, \boldsymbol{v}')$ , as the Hellinger distance between the previously estimated FOD (represented on a dense grid specified by  $\tilde{\boldsymbol{\Phi}}$ ) in voxel  $\boldsymbol{v}$ ,  $\hat{\boldsymbol{f}}_{d_{s-1}}(\boldsymbol{v}) := \tilde{\boldsymbol{\Phi}} \boldsymbol{C} \hat{\boldsymbol{\beta}}_{d_{s-1}}(\boldsymbol{v}) / ||\tilde{\boldsymbol{\Phi}} \boldsymbol{C} \hat{\boldsymbol{\beta}}_{d_{s-1}}(\boldsymbol{v})||_2$ , and the previously estimated FOD in voxel  $\boldsymbol{v}'$ ,  $\hat{\boldsymbol{f}}_{d_{s-1}}(\boldsymbol{v}') := \tilde{\boldsymbol{\Phi}} \boldsymbol{C} \hat{\boldsymbol{\beta}}_{d_{s-1}}(\boldsymbol{v}') / ||\tilde{\boldsymbol{\Phi}} \boldsymbol{C} \hat{\boldsymbol{\beta}}_{d_{s-1}}(\boldsymbol{v}')||_2$ . Following the formula of Hellinger distance,  $\mathrm{Dist}_s(\boldsymbol{v}, \boldsymbol{v}')$  can be expressed as

$$\operatorname{Dist}_s(oldsymbol{v},oldsymbol{v}') := rac{1}{\sqrt{2}} \left\| \sqrt{\hat{oldsymbol{f}}_{d_{s-1}}(oldsymbol{v})} - \sqrt{\hat{oldsymbol{f}}_{d_{s-1}}(oldsymbol{v}')} 
ight\|_2,$$

where the square root of vector is applied element-wisely. The Hellinger distance measures specifically on distribution functions such as FOD. Compared with a commonly used distance, the  $l_2$  distance, the Hellinger distance includes the square root operation in its formula which emphasizes more on the peak values of distribution functions. As a result, a single fiber voxel will probably be more similar to its single fiber neighbors rather than its crossing fiber neighbors, so that the signals from crossing fiber neighbors may not affect the smoothing procedure of this single fiber voxel too much. On the other side, a crossing fiber voxel can be limitedly influenced by the signals from its single fiber neighbors as well. In this case, the transferral of neighborhood information is more targeted and efficient, and the boundary between the estimated single fiber region and crossing fiber region will be more distinct.

# 3.2 Weight rescaling

The proposed weight  $\omega_{d_s}(\boldsymbol{v}, \boldsymbol{v}')$ , however, does not handle the extreme cases very well. For example, if the FOD estimate at voxel  $\boldsymbol{v}$  is already well-smoothed, when  $d_s$  increases, both the location weight  $\omega_{\text{loc},d_s}(\boldsymbol{v},\boldsymbol{v}')$  and the similarity weight  $\omega_{\text{sim},d_s}(\boldsymbol{v},\boldsymbol{v}')$  for  $\boldsymbol{v}' \in N_{d_s}(\boldsymbol{v})$  increase (the increment of  $\omega_{\text{sim},d_s}(\boldsymbol{v},\boldsymbol{v}')$  is due to the increment of similarity within neighborhood), which somewhat overemphasizes the smoothness nature and results in potential

over-smoothing. On the contrary, for badly-smoothed FOD estimate at voxel  $\boldsymbol{v}$ , we expect it would largely incorporate its neighborhood's information to make the estimation consistent with its neighbors. However when  $d_s$  increases,  $\omega_{\text{sim},d_s}(\boldsymbol{v},\boldsymbol{v}')$  does not increase too much due to the dissimilarities between voxel  $\boldsymbol{v}$  and its neighbor  $\boldsymbol{v}'$ , and is usually much lower than those weights on well-smoothed voxels, which in some degree overlooks the smoothness nature and leads to potential under-smoothing.

Our proposed NARM method can well adjust these extreme smoothing circumstances. The main idea is that we rescale the similarity weight  $\omega_{\text{sim},d_s}(\boldsymbol{v},\boldsymbol{v}')$  so that it is not very sensitive to those extreme cases. Specifically, at step s, we calculate the minimum value among the Hellinger distances between the estimated FOD in voxel v and the estimated FODs in its nearest neighboring voxels  $\{v': ||v-v'||_2 = 1\}$ , which are the nearest four voxels (left, right, top, bottom) in two-dimensional region or six voxels (left, right, top, bottom, front, end) in three-dimensional region. We denote this minimum nearest-neighbor distance as MNN-Dist<sub>s</sub>( $\boldsymbol{v}$ ) :=  $\min_{\boldsymbol{v}':||\boldsymbol{v}-\boldsymbol{v}'||_2=1} \mathrm{Dist}_s(\boldsymbol{v},\boldsymbol{v}')$ . Due to the smoothness nature of the HARDI data, it is natural to assume that each voxel has at least one similar nearest neighbor. In this case, a relatively large value of MNN-Dist<sub>s</sub>( $\mathbf{v}$ ) may indicate under-smoothness and a relatively small value may indicate well-smoothness or over-smoothness. Thus, if we set MNN-Dist $_s^{\alpha}$  to be the  $\alpha$  percentile of MNN-Dist $_s(v)$ across all voxels  $\boldsymbol{v}$ , then for those  $\alpha$  percent voxels ( $\alpha$  is usually set below 20%) with  $MNN-Dist_s(\boldsymbol{v}) > MNN-Dist_s^{1-\alpha}$ , we need to boost their smoothing procedure since they are considered to be under-smoothed, and we should slow down the smoothing procedure for those  $\alpha$  percent voxels with MNN-Dist<sub>s</sub>( $\boldsymbol{v}$ ) < MNN-Dist<sub>s</sub> since it is very likely that they are already well-smoothed or even over-smoothed.

The detailed method is presented in the following. Suppose for the voxel  $\boldsymbol{v}$ , MNN-Dist $_s(\boldsymbol{v}) = \mathrm{Dist}_s(\boldsymbol{v}, \boldsymbol{u})$ , where  $\boldsymbol{u}$  is one of the nearest neighbor of  $\boldsymbol{v}$ , then  $\mathrm{Dist}_s(\boldsymbol{v}, \boldsymbol{u})$  is set to be MNN-Dist $_s^{1-\alpha}$  if MNN-Dist $_s(\boldsymbol{v}) > \mathrm{MNN-Dist}_s^{1-\alpha}$ , or MNN-Dist $_s^{\alpha}$  if MNN-Dist $_s(\boldsymbol{v}) < \mathrm{MNN-Dist}_s^{\alpha}$ , and all the other  $\mathrm{Dist}_s(\boldsymbol{v}, \boldsymbol{v}')$ ,  $\boldsymbol{v}' \in N_{d_s}(\boldsymbol{v})$ ,  $\boldsymbol{v}' \neq \boldsymbol{u}$ , are decreased/increased proportionally. In other words, the new similarity measure between the estimated FODs in voxels  $\boldsymbol{v}$  and  $\boldsymbol{v}'$  at step s is

$$\widetilde{\mathrm{Dist}}_s(\boldsymbol{v},\boldsymbol{v}') = \mathrm{Dist}_s(\boldsymbol{v},\boldsymbol{v}') \cdot \min \left\{ \frac{\mathrm{MNN-Dist}_s^{1-\alpha}}{\mathrm{MNN-Dist}_s(\boldsymbol{v})}, \ 1 \right\} \cdot \max \left\{ \frac{\mathrm{MNN-Dist}_s^{\alpha}}{\mathrm{MNN-Dist}_s(\boldsymbol{v})}, \ 1 \right\},$$

and the new weight is

$$\omega_{d_s}(\boldsymbol{v}, \boldsymbol{v}') = \frac{K_{\text{loc}}(||\boldsymbol{v} - \boldsymbol{v}'||_2/d_s)K_{\text{sim}}(\widetilde{\text{Dist}}_s(\boldsymbol{v}, \boldsymbol{v}'))}{\sum_{\boldsymbol{v}' \in N_{d_s}(\boldsymbol{v})}K_{\text{loc}}(||\boldsymbol{v} - \boldsymbol{v}'||_2/d_s)K_{\text{sim}}(\widetilde{\text{Dist}}_s(\boldsymbol{v}, \boldsymbol{v}'))}.$$

Here we can see that, for those under-smoothed voxels with MNN-Dist<sub>s</sub>( $\boldsymbol{v}$ ) > MNN-Dist<sub>s</sub><sup>1- $\alpha$ </sup>, we have  $\widetilde{\mathrm{Dist}}_s(\boldsymbol{v},\boldsymbol{v}')$  < Dist<sub>s</sub>( $\boldsymbol{v},\boldsymbol{v}'$ ) and thus an increased similarity weight, which could effectively accelerate the smoothing procedure. On the contrary, for those already well-smoothed or even over-smoothed voxels, we have a decreased similarity weight leading to the deceleration of the smoothing procedure.

## 3.3 Stopping rule

A stopping rule is also essential in NARM to prevent potential over-smoothing. Our proposed stopping rule is based on the minimum nearest-neighbor distance MNN-Dist<sub>s</sub>(v) as well, and the basic idea is that we terminate smoothing procedure for voxel v when MNN-Dist<sub>s</sub>(v) stops decreasing as s increases. Concretely, when we observe min{MNN-Dist<sub>s</sub>(v), MNN-Dist<sub>s-1</sub>(v)}  $\geq$  MNN-Dist<sub>s-2</sub>(v), we stop the smoothing procedure for voxel v and set  $\hat{\beta}_{d_{s'}}(v) = \hat{\beta}_{d_{s-2}}(v)$  for  $s' \geq s-1$ . The intuition behind this stopping rule is straightforward: when MNN-Dist<sub>s</sub>(v) stops decreasing, the extent of similarity between voxel v and its neighbors cannot be improved anymore, which means voxel v has already been well-smoothed and the smoothing procedure should be terminated for voxel v to prevent over-smoothing. In practice, the smoothing procedure for different voxels may stop at different steps, indicating the heterogeneity nature of the degree of smoothness across the voxel region.

The computation costs of weight calculation and stop checking are both much cheaper than the cost of FOD estimation by SN-lasso. Hence, compared with voxel-wise FOD estimation method when applied across all voxels, the NARM method costs at most S times more, where S is the total number of smoothing steps. In fact, the cost can be much less than S times in practice (usually around S/2 times), since no FOD estimation is required if the smoothing procedure of the voxel is already terminated by the stopping rule.

### 3.4 Related works

Rao et al. (2016) proposed *Penalized Multiscale Adaptive Regression Model* (PMARM) for spatial and adaptive estimation of ODF. As a general smoothing framework, it can be easily migrated to FOD estimation. Similar to NARM, PMARM also replaces the single diffusion measurement within each voxel by the weighted average of diffusion measurements, adaptively updates the weights within nested neighborhoods with increasing radius, and uses a stopping rule to avoid over-smoothing. However, PMARM has three major drawbacks compared with our method. Here for convenience, we use the same notations in PMARM as those in our NARM method.

Firstly, the similarity measure  $\operatorname{Dist}_s(\boldsymbol{v},\boldsymbol{v}')$  in PMARM is defined as the  $l_2$  distance between the previously estimated FODs at voxel  $\boldsymbol{v}$  and  $\boldsymbol{v}'$ , whereas in our method, the Hellinger distance is used for calculating the similarity measure. As pointed out before, compared with the Hellinger distance, the  $l_2$  distance performs less effectively in quantifying the similarity between estimated FODs. Specifically, the  $l_2$  distance may struggle in distinguishing the single fiber voxel and crossing fiber voxel, resulting in blurred boundary between the estimated single fiber region and crossing fiber region, since spurious signals could be transferred more easily between these two regions. As a consequence, we may have difficulties in the following fiber orientation detection and fiber tracking.

The second drawback is that PMARM does not cover the rescaling process for the similarity weight  $\omega_{\sin,d_s}(\boldsymbol{v},\boldsymbol{v}')$ . As mentioned before, some extreme cases may not be well treated by PMARM. For example, for those already well-smoothed voxels, the weights seem to overemphasize the smoothness nature and may lead to over-smoothing. On the other hand, the weights of those under-smoothed voxels seem too low to incorporate enough neighborhood information and may lead to under-smoothing.

Finally, PMARM uses a different stopping rule. At step s, let  $\mathrm{Dist}_s(\boldsymbol{v})$  denote the  $l_2$  distance between previously estimated FOD  $\hat{f}_{d_{s-1}}(\boldsymbol{v})$  and currently estimated FOD  $\hat{f}_{d_s}(\boldsymbol{v})$ . Rao et al. (2016) states that, if  $\mathrm{Dist}_s(\boldsymbol{v}) > c_s$ , where  $c_s$  is a pre-specified positive scalar, then some "bad" signals from neighborhood voxels may be incorporated and lead to a significant change in the estimated FOD, and we thus should stop the smoothing procedure and set  $\hat{\beta}_{d_s}(\boldsymbol{v}) = \hat{\beta}_{d_{s-1}}(\boldsymbol{v})$  and s = S for the voxel  $\boldsymbol{v}$ . On the contrary, if  $\mathrm{Dist}_s(\boldsymbol{v}) \leq c_s$ , we continue

with the smoothing procedure for the voxel  $\mathbf{v}$ . In practice,  $c_s$  is set as  $\chi^2(1)^{0.6/s}c$ , where  $\chi^2(1)^{\alpha}$  is the upper  $\alpha$  percentile of the  $\chi^2(1)$  distribution, and c is a positive scalar, which is chosen to be the median of  $\mathrm{Dist}_0(\mathbf{v}, \mathbf{v}')$  where  $\mathbf{v}$  and  $\mathbf{v}'$  are preselected voxels.

However, as pointed out by Rao et al. (2016), in practice it can be very difficult to determine a good  $c_s$  value. Actually, it is hard to determine a global criterion based on a uniform measure such as  $\chi^2(1)^{0.6/s}c$  which fits every voxels well. In some voxels where the original FOD estimates are quite reasonable, the FOD estimations can become over-smoothed very quickly, however the global stopping rule may not be able to stop the smoothing procedure in time. While in some other voxels where the FODs are not originally well-estimated, they could have a long way towards good estimates, whereas the global stopping rule may stop the smoothing procedure too early.

In fact, the selection of stopping rule is crucial in spatial smoothing method, and extensive simulation results show that the ultimate FOD estimates are quite sensitive to the hyper-parameter selection in the stopping rule. However, in the expression of  $c_s$ :  $\chi^2(1)^{0.6/s}c$ , the  $\chi^2$  distribution is actually not justifiable, and the tuning parameter selection (both the percentile of  $\chi^2$  distribution and the constant value c) is somewhat ad-hoc in practice, where the way of preselecting voxels used in estimating c value is not described in detail. Compared with the stopping rule in PMARM, the stopping rule in NARM based on minimum nearest-neighbor distance is more reasonable and applicable, where no additional hyperparameters are needed to be tuned. The essential difference between these two methods is that instead of using a global criterion based on a uniform measure, we use a local criterion adjusted to each voxel, thus can well handle different smoothing cases for different voxels.

# 3.5 Further extension: multiple b-values

In this section, we briefly introduce a simple but powerful extension of the SN-lasso method, which can be easily incorporated into our NARM method. Recall that the original SN-lasso is built on diffusion weighted signals sampled with a single b-value. However, in many recent D-MRI dataset such as the WU-Minn Human Connectome Project (HCP) database (Van Essen et al. 2013), the diffusion weighted signals are sampled with multiple b-values. Specifically, a list of b-values  $\{b_k\}_{k=1,\ldots,K}$  is pre-specified. For each b-value  $b_k$ ,

we have its corresponding observed diffusion weighted measurements  $\mathbf{y}_k(\mathbf{v}) = \{y_{ki}(\mathbf{v})\}_{i=1}^{n_k}$  based on  $n_k$  gradient directions. Using the original SN-lasso, we model the measurements  $\mathbf{y}_k(\mathbf{v})$  as:

$$y_k(v) = \Phi_k R_k C \beta(v) + \epsilon_k, \tag{6}$$

where  $\Phi_k$  is an  $n_k \times L$  matrix constructed on the  $n_k$  gradient directions,  $R_k$  is an  $L \times L$  diagonal matrix based on the *b*-value  $b_k$ , C is an  $L \times N$  matrix independent with  $b_k$ ,  $\boldsymbol{\beta}(\boldsymbol{v})$  is an  $N \times 1$  vector of FOD's SN coefficients to be estimated, and  $\epsilon_k$  is an  $n_k \times 1$  error vector.

To combine the sampled diffusion signals from K different b-values, a straightforward way is to combine the K linear models (6) by stacking the response vectors, design matrices and error vectors. Let  $\tilde{n} = \sum_{k=1}^{K} n_k$ ,  $\tilde{\boldsymbol{y}}(\boldsymbol{v}) = (\boldsymbol{y}_1(\boldsymbol{v})^T, \dots, \boldsymbol{y}_K(\boldsymbol{v})^T)^T$  be an  $\tilde{n} \times 1$  response vector,  $\tilde{\boldsymbol{D}} = ((\boldsymbol{\Phi}_1 \boldsymbol{R}_1 \boldsymbol{C})^T, \dots, (\boldsymbol{\Phi}_K \boldsymbol{R}_K \boldsymbol{C})^T)^T$  be an  $\tilde{n} \times N$  design matrix and  $\tilde{\boldsymbol{\epsilon}}(\boldsymbol{v}) = (\boldsymbol{\epsilon}_1(\boldsymbol{v})^T, \dots, \boldsymbol{\epsilon}_K(\boldsymbol{v})^T)^T$  be an  $\tilde{n} \times 1$  error vector. The combination of the K linear models becomes:

$$\tilde{\mathbf{y}}(\mathbf{v}) = \tilde{\mathbf{D}}\boldsymbol{\beta}(\mathbf{v}) + \tilde{\boldsymbol{\epsilon}}.$$
 (7)

Now the FOD's SN coefficients  $\beta(v)$  can be estimated by

$$\hat{\boldsymbol{\beta}}(\boldsymbol{v}) = \arg\min_{\boldsymbol{\beta}(\boldsymbol{v}): \tilde{\boldsymbol{\Phi}}\boldsymbol{C}\boldsymbol{\beta}(\boldsymbol{v}) \succeq \boldsymbol{0}} \frac{1}{2} ||\tilde{\boldsymbol{y}}(\boldsymbol{v}) - \tilde{\boldsymbol{D}}\boldsymbol{\beta}(\boldsymbol{v})||_{2}^{2} + \lambda ||\boldsymbol{\beta}(\boldsymbol{v})||_{1}.$$
(8)

We can see that, compared with the original SN-lasso using signals sampled from a single b-value, more samples can be included in the extended SN-lasso, therefore the statistical efficiency in estimating  $\beta(v)$  is improved and its variation is decreased. Simulation results in the next section will show that, by stacking the responses and design matrices for different b-values, the FOD estimation result becomes not only more accurate than the result based on a single b-value, but also more robust to the selection of tuning parameter  $\lambda$  in  $l_1$  penalty.

# 4 Synthetic experiments

In this section, we use extensive simulation studies based on two-dimensional and three-dimensional regions of interest (ROIs) with synthetic D-MRI data to evaluate the performance of our proposed NARM method, and to compare it with other FOD estimation methods including the voxel-wise SN-lasso method and the PMARM method.

## 4.1 Simulation setup

In ROIs, we simulate the noiseless diffusion weighted signals according to the spherical convolution model (1). For voxels with at least one fiber bundles, the true FOD function is constructed by a weighted summation of dirac functions:  $F(\theta, \phi) = \sum_{k=1}^{K} p_k \delta_{\theta_k, \phi_k}(\theta, \phi)$ ,  $\theta \in [0,\pi], \ \phi \in [0,2\pi),$  with  $p_k$  being the volume fraction of the k-th fiber bundle and  $(\theta_k, \phi_k)$  being the spherical coordinate of k-th fiber direction. In our simulation studies, we set  $p_1 = p_2 = 0.5$  for voxels with two fiber bundles. For voxels with zero fiber bundles (i.e., isotropic diffusion), the true FOD function is constant on the sphere:  $F(\theta, \phi) = 1/(4\pi)$ . The response function is built based on the single tensor model (Le Bihan & Warach 1995, Basser & Jones 2002, Mori 2007):  $R(\cos(\theta)) = S_0 \exp(-b(\lambda_1 \sin^2 \theta + \lambda_3 \cos^2 \theta)), \quad \theta \in [0, \pi],$ where we set  $S_0 = 1$ , b-value  $b = 1000 s / mm^2$  or  $3000 s / mm^2$ ,  $\lambda_1 = 10^{-3} mm^2 / s$ , and the ratio between  $\lambda_3$  and  $\lambda_1$  as 10 for voxels with at least one fiber bundles and 1 for voxels with zero fiber bundles throughout our simulation studies. We generate the noiseless diffusion weighted signals along n gradient directions, where the gradient directions are based on the icosphere meshes and n is set to be either 41 or 81. Finally, we add independent Rician noise (Gudbjartsson & Patz 1995, Hahn et al. 2006) to the noiseless diffusion weighted signals to generate the simulated diffusion weighted measurements. The signal-to-noise ratio SNR =  $S_0/\sigma$ , where  $\sigma$  is the Rician noise level, is set to be 20 in our simulation studies.

In the simulation studies, we generate true fiber directions and their corresponding observed diffusion weighted measurements on a two-dimensional or three-dimensional voxel grid. These fiber directions are changing smoothly across voxels, and within each voxel, there is either one dominant fiber direction, or two crossing fiber directions, or no fiber directions at all (i.e., isotropic diffusion). We estimate the FOD at each voxel by using several FOD estimation methods. Specifically, in 2D ROI simulations, we conduct a comprehensive exploration of the FOD estimation methods, including the voxel-wise SN-lasso method (referred to as SN-lasso(voxel-wise)), the NARM method with different selections of  $\alpha$  in weight rescaling (referred to as NARM( $\alpha = \alpha_0$ )), the NARM method with certain components missing (referred to as NARM(no stopping&rescaling), NARM(no stopping) and NARM(no rescaling)), the NARM method with the stopping rule replaced by the one in PMARM (referred

to as NARM( $\chi^2$ -stopping,  $c = c_0$ )), and the PMARM method with different selections of c in stopping rule (referred to as PMARM( $c = c_0$ )). We also include the voxel-wise SN-lasso method applied on the noiseless diffusion signals (referred to as SN-lasso(noiseless)) as a gold standard. In 3D ROI simulations, for convenience, we only focus on a small set of FOD estimation methods which are representative of the aforementioned methods. Fiber peaks can be further extracted from the estimated FODs by using the peak detection algorithm proposed in Yan et al. (2018).

We use a variety of numerical metrics to examine the performance of each method. They include: (1) The proportions of voxels where the number of detected fiber bundles are either correct, over-estimated or under-estimated, reported under "Co.", "Ov." and "Un." respectively in the tables. (2) Among the "correct" voxels, the median angular error between the identified fiber direction(s) and true fiber direction(s), shown under "Err." in the tables. (3) The mean and standard deviation (across all voxels in ROI) of the Hellinger distance between the estimated FOD and the true FOD (the true FOD function projected onto an SH basis with  $l_{\text{max}} = 8$ ), and between the estimated FOD and the estimated FOD from noiseless signals. They are shown under "Mean H-dist." and "SD H-dist." in the tables.

#### 4.2 2D ROI simulation I

In the first simulation study of ROI, we generate two fiber bundles on a  $10 \times 10$  2D voxel grid, where one-fiber voxels (72 such voxels) and two-fiber voxels (28 such voxels) are included. Figure 1(a) shows the true FODs represented by  $l_{\text{max}} = 8$  SH basis on this 2D ROI. We can see clearly the two fiber bundles, where one is from the top left to the bottom right, and the other is from the top right to the bottom left, with the crossing fiber region in the middle of the ROI. We set the b-value  $b = 1000s/mm^2$  and the number of gradient directions n = 41. In some real datasets, the b-values and the numbers of gradient directions may be larger than our settings here, leading to less challenging FOD estimation problems. However, the goal of this simulation study is to examine the performance of various FOD estimation methods and reveal the effectiveness of each component in the smoothing procedure, thus using the relatively difficult case can help our understanding

better. We refer to this simulation as the 2D ROI simulation I.

We examine the performance of FOD estimation methods listed in Section 4.1. Specifically, we set  $\alpha_0 \in \{0.10, 0.15, 0.20\}$  in NARM( $\alpha = \alpha_0$ ),  $c_0 \in \{3,4\}$  in NARM( $\chi^2$ -stopping,  $c = c_0$ ), and  $c_0 \in \{0.10, 0.15, 0.20\}$  in PMARM( $c = c_0$ ). Extensive experiments show that the results are not very sensitive to the choice of  $\alpha$  when it varies between 0.1 and 0.2, whereas they are quite sensitive to the choice of c. Here we preselect the values of c which already leads to relatively well-performed results. In practice, c values are not easy to be selected and the c selection approach is somewhat ad-hoc and not described explicitly by Rao et al. (2016). We set  $\gamma = 2$  in  $K_{\text{sim}}(u) = \exp(-\gamma u^2)$  for NARM and  $\gamma = 20$  for PMARM (adjusted for scale difference).

Figure 1(b)-(f) present the estimated FOD images on the ROI. In general, the FOD estimates with smoothing procedure (Figure 1(c)-(f)) significantly outperform the voxel-wise FOD estimates (Figure 1(b)) in terms of recovering the consistently orientated FODs across voxels especially in the crossing fiber region and removing the spurious peaks. The NARM estimates without stopping rule and weight rescaling (Figure 1(d)) seem heavily over-smoothed, where the boundary between single fiber region and crossing fiber region looks unclear. Compared with the PMARM estimates (Figure 1(e)(f)), the NARM estimates (Figure 1(c)) perform better in identifying the peak directions. For example, only the NARM estimates can successfully recover the crossing fiber structure in the voxel (6, 9) (assume the coordinates of the voxel in the bottom left is (0, 0)), which seems very challenging to recover due to its small crossing angle and its boundary location between single fiber region and crossing fiber region. Take single fiber voxels (1, 6) and (10, 6) as another example. the NARM method leads to much less noisy estimates than the PMARM method does, where the PMARM estimates seem to misidentify these two single fiber voxels as crossing fiber voxels.

Table 1 and S.1 (Table S.1 is in the Supplementary Material) present the quantitative summaries of the FOD estimation accuracy by using the success rate&angular error and the Hellinger distance respectively, where the detailed description can be found in Section 4.1. We can see that the NARM estimates are not very sensitive to the selection of  $\alpha$  (the proportion of extreme cases whose weights need to be rescaled), and  $\alpha = 0.15$  performs best due to its lowest median angular error in the 2-fiber cases. Both tables reveal that

the NARM estimates substantially reduce the failure rates, median angular errors and mean Hellinger distances from the voxel-wise SN-lasso estimates, indicating that NARM is able to efficiently exploit the spatial smoothness and reduce noise for better peak detection and angle estimation. Compared with the PMARM estimates with three preselected c values in stopping rule, NARM outperforms all of them due to its perfect success rates among both 1-fiber and 2-fiber voxels and smaller mean Hellinger distances, whereas PMARM seems to have blurred boundary between single fiber region and crossing fiber region due to its relatively high proportion of over-estimated 1-fiber voxels and under-estimated 2-fiber voxels. Finally, if the stopping rule is not implemented, the NARM estimates will have significantly lower successful rates and larger angular errors in the 1-fiber cases due to over-smoothing. Even if we replace the original stopping rule in NARM by the stopping rule from PMARM (referred to as  $\chi^2$ -stopping) with preselected c values, it is still less effective in distinguishing the single fiber region and crossing fiber region, indicating the superior performance of the stopping rule in NARM not only in higher estimation accuracy but also in more convenient estimation process (with no hyper-parameters hard to tune in practice).

Figure 1: **2D ROI simulation I**: FOD estimates. (a) True FODs in SH basis with  $l_{\rm max}=8$ ; (b) SN-lasso (voxel-wise) estimates; (c) NARM ( $\alpha=0.15$ ) estimates; (d) NARM (no stopping&rescaling) estimates; (e) PMARM (c=0.15) estimates; (f) PMARM (c=0.20) estimates.

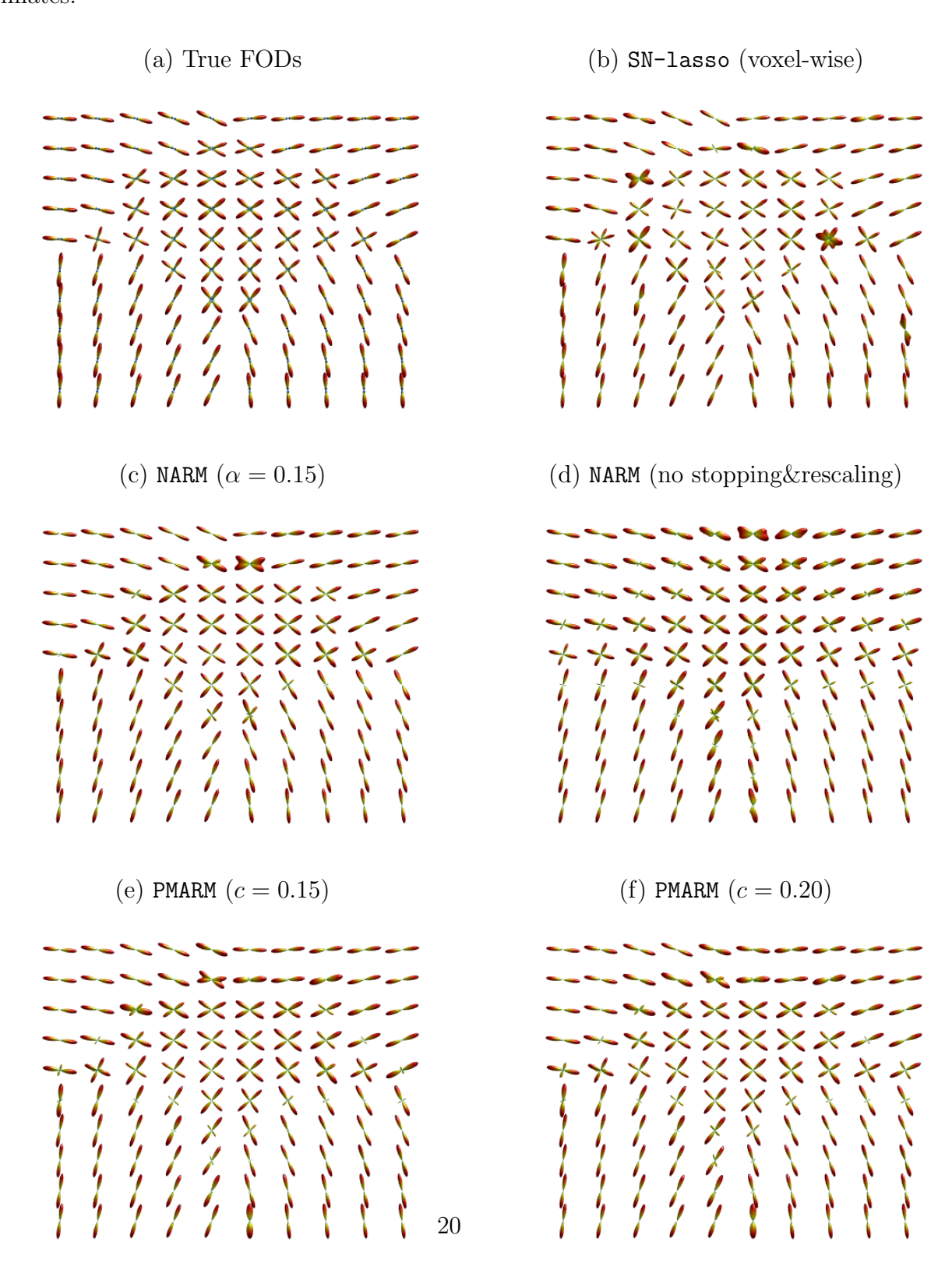


Table 1: **2D ROI simulation I**: Success rate and angular error.

	1 D'1		0 17:1	
	1-Fiber		2-Fiber	
Estimator	Co./Ov./Un.	Err.	Co./Ov./Un.	Err.
${\tt SN-lasso}({\tt noiseless})$	1.00/0.00/0.00	1.55	1.00/0.00/0.00	1.00
${\tt SN-lasso}({\tt voxel-wise})$	1.00/0.00/0.00	2.62	0.78/0.18/0.04	8.51
$\mathtt{NARM}(\alpha=0.10)$	1.00/0.00/0.00	2.61	1.00/0.00/0.00	3.81
$\mathtt{NARM}(\alpha=0.15)$	1.00/0.00/0.00	2.61	1.00/0.00/0.00	3.59
$\mathtt{NARM}(\alpha=0.20)$	1.00/0.00/0.00	2.61	1.00/0.00/0.00	3.72
${\tt NARM} ({\tt no\ stopping\&rescaling})$	0.81/0.19/0.00	5.34	0.96/0.04/0.00	3.09
NARM(no stopping)	0.76/0.24/0.00	4.62	0.96/0.04/0.00	3.04
NARM(no rescaling)	1.00/0.00/0.00	2.61	1.00/0.00/0.00	3.81
$\mathtt{NARM}(\chi^2\text{-stopping},c=3)$	0.97/0.03/0.00	2.69	0.93/0.03/0.04	3.72
$\mathtt{NARM}(\chi^2\text{-stopping},c=4)$	0.94/0.06/0.00	2.72	0.96/0.00/0.04	3.34
PMARM(c=0.15)	0.93/0.07/0.00	2.53	0.96/0.00/0.04	4.08
$\mathtt{PMARM}(c=0.20)$	0.92/0.08/0.00	2.61	0.96/0.00/0.04	3.44
$\mathtt{PMARM}(c=0.25)$	0.89/0.11/0.00	2.64	0.96/0.00/0.04	3.44

#### 4.3 2D ROI simulation II

In the second simulation study of ROI (2D ROI simulation II), two fiber bundles are generated on a  $10 \times 10$  2D voxel grid, including 22 zero-fiber (isotropic) voxels, 66 one-fiber voxels and 12 two-fiber voxels. The true FODs represented by  $l_{\text{max}} = 8$  SH basis are shown in Figure 2(a). We still set the *b*-value  $b = 1000s/mm^2$  and the number of gradient directions n = 41.

In Figure 2 and Table 2, S.2 (Table S.2 is in the Supplementary Material), we focus on the FOD reconstruction results particularly on the zero-fiber (isotropic) regions. As can be seen from Figure 2, the NARM estimates (Figure 2(c)) and the PMARM estimates with c=0.05 (Figure 2(e)) can identify more consistent zero-fiber regions than the voxel-wise SN-lasso estimates (Figure 2(b)) do, where the isotropic structures in the voxels (6, 2) and (10, 6)

are successfully recovered by these two estimates. Moreover, NARM outperforms PMARM due to its perfect success rate and much lower median angular error in recovering the crossing fiber region as well as its lower mean Hellinger distance. Note that the PMARM estimates with c=0.10 (Figure 2(f))) perform much worse than the PMARM estimates with c=0.05 (Figure 2(e)) in terms of successful rate in zero-fiber region, indicating the difficulty in c selection for PMARM in practice. Finally, removing stopping rule and weight rescaling from NARM will result in serious over-fitting problem, where no zero-fiber voxels are detected, as shown in Figure 2(d). Replacing the original stopping rule in NARM by the  $\chi^2$  stopping rule from PMARM will worsen the success rate of FOD reconstruction in all three regions with zero fiber voxels, single fiber voxels and crossing fiber voxels.

Figure 2: **2D ROI simulation II**: FOD estimates. (a) True FODs in SH basis with  $l_{\rm max}=8$ ; (b) SN-lasso (voxel-wise) estimates; (c) NARM ( $\alpha=0.15$ ) estimates; (d) NARM (no stopping&rescaling) estimates; (e) PMARM (c=0.05) estimates; (f) PMARM (c=0.10) estimates.

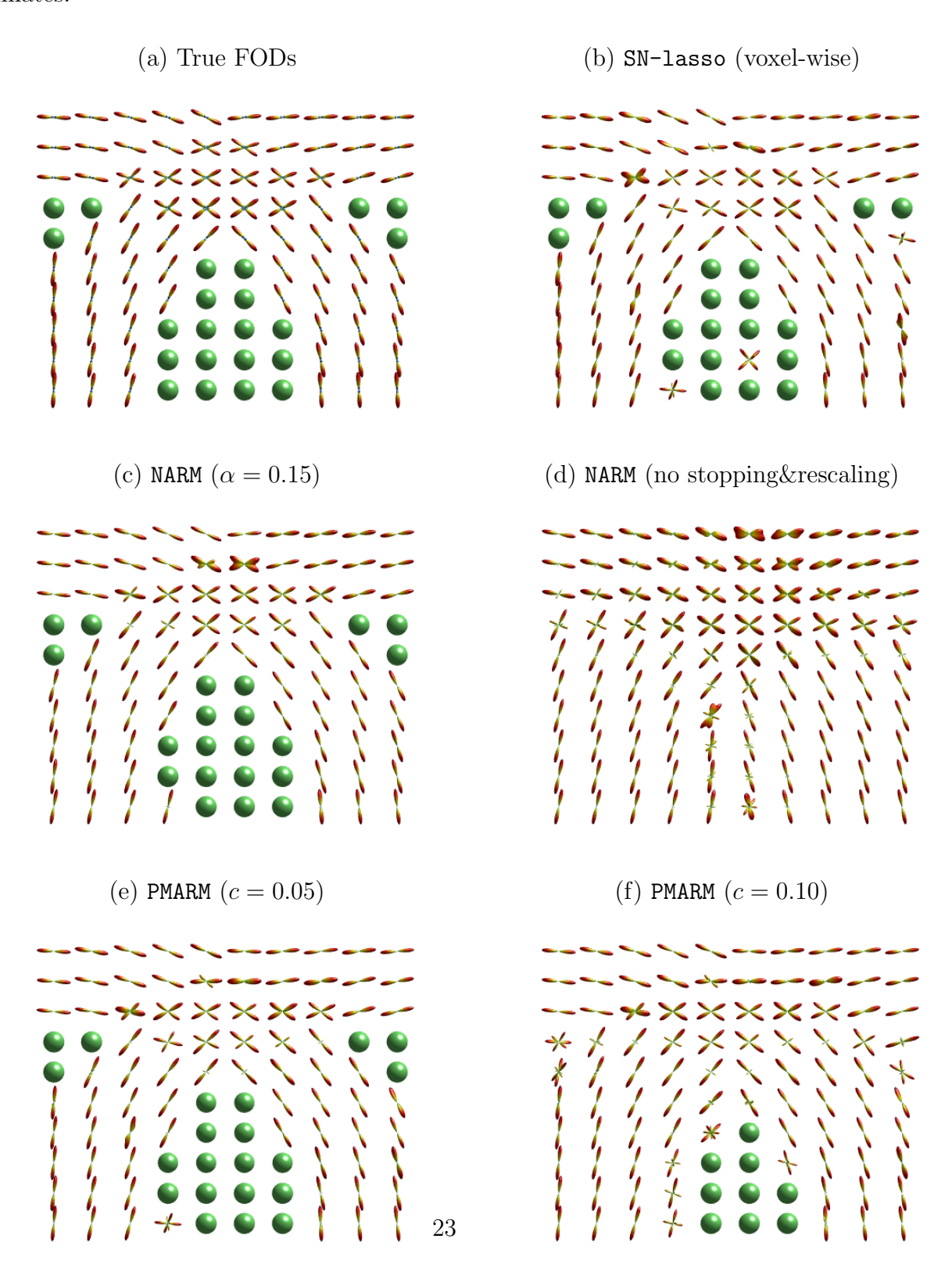


Table 2: 2D ROI simulation II: Success rate and angular error.

	0-Fiber	1-Fiber		2-Fiber		
Estimator	Co./Ov.	Co./Ov./Un.	Err.	Co./Ov./Un.	Err.	
SN-lasso(noiseless)	1.00/0.00	1.00/0.00/0.00	1.92	1.00/0.00/0.00	1.00	
${\tt SN-lasso}(voxel\text{-}wise)$	0.86/0.14	1.00/0.00/0.00	2.72	0.92/0.00/0.08	8.88	
$\overline{\hspace{1cm} \mathtt{NARM}(\alpha=0.10)}$	0.95/0.05	1.00/0.00/0.00	2.93	1.00/0.00/0.00	4.76	
$\mathtt{NARM}(\alpha=0.15)$	0.95/0.05	1.00/0.00/0.00	2.86	1.00/0.00/0.00	4.76	
$\mathtt{NARM}(\alpha=0.20)$	0.95/0.05	0.98/0.02/0.00	2.86	1.00/0.00/0.00	4.76	
NARM(no stopping&rescaling)	0.00/1.00	0.79/0.21/0.00	4.00	1.00/0.00/0.00	4.37	
NARM(no stopping)	0.68/0.32	0.79/0.21/0.00	4.18	1.00/0.00/0.00	3.70	
NARM(no rescaling)	0.95/0.05	1.00/0.00/0.00	2.93	1.00/0.00/0.00	4.76	
$\mathtt{NARM}(\chi^2\text{-stopping},c=2)$	0.73/0.27	0.97/0.03/0.00	2.48	0.92/0.00/0.08	5.69	
$\mathtt{NARM}(\chi^2\text{-stopping},c=3)$	0.73/0.27	0.95/0.05/0.00	2.57	0.92/0.00/0.08	4.28	
$\mathtt{NARM}(\chi^2\text{-stopping},c=4)$	0.73/0.27	0.94/0.06/0.00	2.57	0.92/0.00/0.08	3.70	
$\boxed{ \text{PMARM}(c=0.05) }$	0.95/0.05	1.00/0.00/0.00	2.57	0.92/0.00/0.08	6.87	
$\mathtt{PMARM}(c=0.10)$	0.41/0.59	0.97/0.03/0.00	2.55	0.92/0.00/0.08	6.41	

#### 4.4 3D ROI simulation

In the third simulation study (3D ROI simulation), we generate two fiber bundles on a  $10 \times 10 \times 5$  3D voxel grid, where 52 zero-fiber voxels, 163 one-fiber voxels and 285 two-fiber voxels are included. Figure S.1(a) shows the true FODs represented by  $l_{\rm max}=8$  SH basis on the 5 z-slices of the 3D ROI. Figure S.1(b) presents the fiber tracts based on the true FODs within the entire 3D ROI. Two fiber bundles can be easily recognized from these plots, where one follows top left to bottom right, into to out-of-page direction, and the other follows top right to bottom left, into to out-of-page direction. We consider b-value at  $b=1000s/mm^2$  and  $3000s/mm^2$ , and the number of gradient directions n=41. Based on the simulation results in previous sections, we select a subset of representative FOD estimation methods for further examination in this simulation study, including the voxel-wise SN-lasso method, the NARM method with  $\alpha=0.15$ , the NARM method without stopping

and rescaling, and the PMARM method with c = 0.05 and c = 0.10. In NARM, we set  $\gamma = 2$  in  $K_{\text{sim}}(u) = \exp(-\gamma u^2)$  at  $b = 1000s/mm^2$  and  $\gamma = 4$  at  $b = 3000s/mm^2$ . The intuition is that we need to slightly slow down the smoothing process as b-value increases, since stronger diffusion signals from larger b-value can themselves lead to better FOD estimates, and no smoothing process as intensive as that for weak diffusion signals is needed.

In the main text, we only report part of the simulation results at  $b = 1000s/mm^2$ . For other results at  $b = 1000s/mm^2$  and the results at  $b = 3000s/mm^2$ , see Sections S.1.3 and S.1.4 of the Supplementary Material, respectively. We can see from Figure 3, S.2 and Table 3, S.3 (Table S.3 is in the Supplementary Material) that the NARM method leads to the most reasonable reconstruction of FODs: It has nearly perfect success rates among 0-fiber, 1-fiber and 2-fiber voxels, the lowest median angular errors, and the smallest mean Hellinger distance. Among the other methods, the voxel-wise SN-lasso method performs poorly in accurate detection of peak direction in crossing fiber region, the PMARM method does not deal with many challenging cases very well and results in less faithful recovery of FODs in terms of success rate and angular error, and the NARM method without stopping and rescaling tends to heavily over-smooth the zero fiber and single fiber regions and results in noisy estimates of FODs with a number of spurious peaks.

We use the tractography results in Figure S.3 to further illustrate and justify our findings. To reconstruct the fiber trajectories, we use the peak detection algorithm (Yan et al. 2018) to extract peaks from the estimated FODs and then apply the deterministic tracking algorithm (Wong et al. 2016) to the extracted peaks. In Figure S.3, the fiber tracts are colored by a RGB color model with red for left-to-right, green for up-to-down and blue for into-to-out-of-page. We also report the total number of fiber tracts and the median of fiber lengths in Figure S.3. As can be seen from Figure S.3, the tracking result based on the NARM method (Figure S.3(c)) seems to be the closest to the underlying truth (Figure S.3(a)), where it shows very clear fiber crossing region with almost no redundant fiber tracts. This implies that the NARM method is able to efficiently exploit the spatial smoothness nature and reduce noise for more accurate fiber orientation detection and angle estimation. On the contrary, the tracking result based on the voxel-wise SN-lasso method (Figure S.3(b)) looks very messy especially in the crossing fiber region, and the small value of its median

fiber length 4.11 indicates the incoherence of fiber directions identified from its FOD estimates. Moreover, both the fiber tracking based on the PMARM method with c = 0.05 and c = 0.10 (Figure S.3(e)(f)) produce more noisy reconstruction of fiber tracts. Finally, Figure S.3(d) shows that many spurious fiber tracts will be generated due to over-smoothing if the NARM method estimates FODs without stopping and rescaling.

For b-value  $b=3000s/mm^2$ , NARM again has visually the best FOD estimates and fiber tracking result, and the highest success rates in all 0-fiber, 1-fiber and 2-fiber regions. See Section S.1.4 of the Supplementary Material for more details. One more thing we notice is that the FOD estimation results from b-value at  $3000s/mm^2$  are better than those from  $1000s/mm^2$ . This indicates that stronger diffusion signals would bring more useful information and lead to more satisfactory FOD reconstruction.

Figure 3: **3D ROI simulation**: FOD estimates on z-slice 2. (a) True FODs in SH basis; (b) SN-lasso (voxel-wise) estimates; (c) NARM ( $\alpha = 0.15$ ) estimates; (d) NARM (no stopping&rescaling) estimates; (e) PMARM (c = 0.05) estimates; (f) PMARM (c = 0.10) estimates.

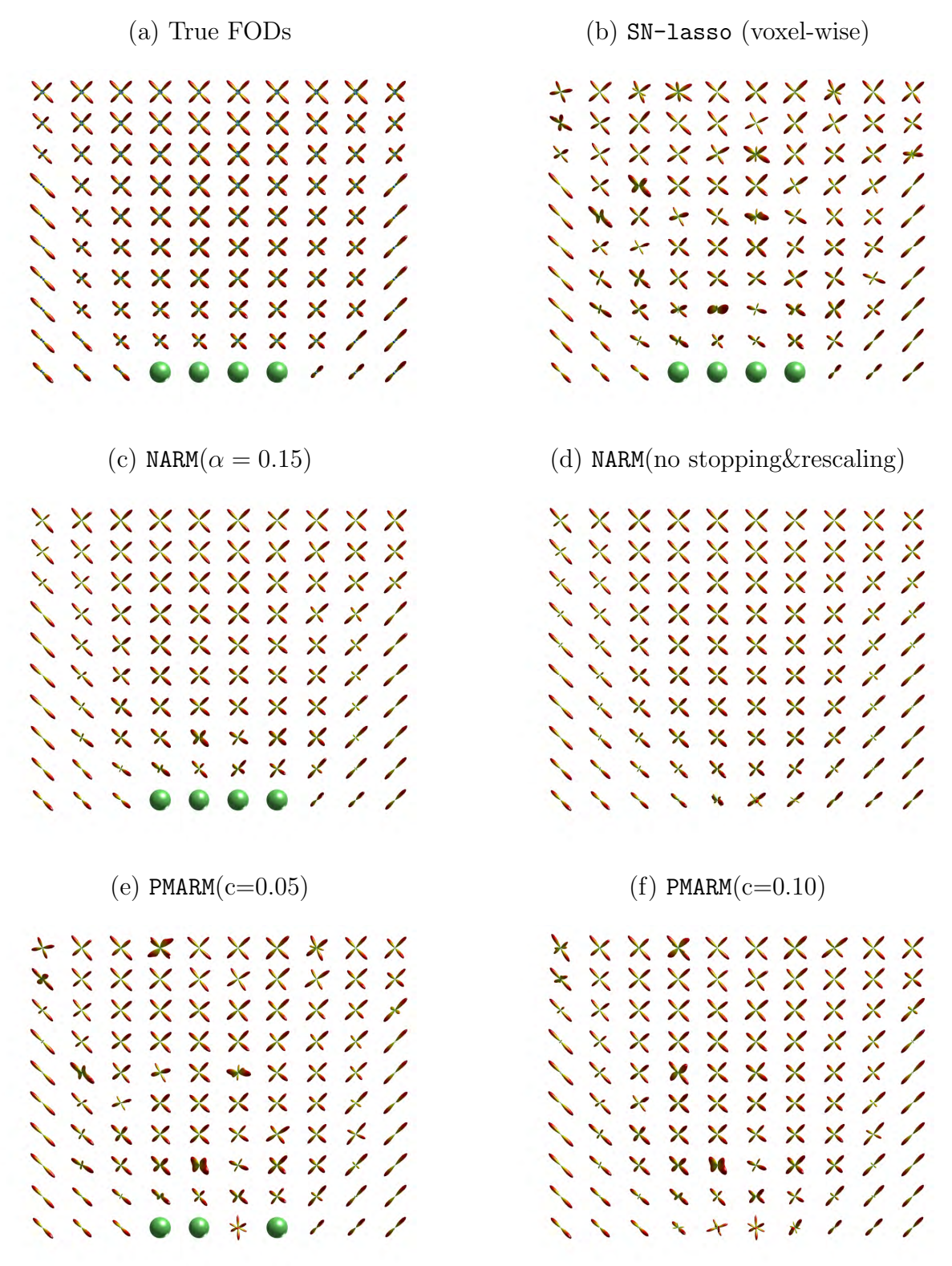


Table 3: **3D ROI simulation**: Success rate and angular error.

	0-Fiber	1-Fiber		2-Fiber		
Estimator	Co./Ov.	Co./Ov./Un.	Err.	Co./Ov./Un.	Err.	
${\tt SN-lasso}({\tt noiseless})$	1.00/0.00	1.00/0.00/0.00	1.61	1.00/0.00/0.00	1.77	
${\tt SN-lasso}({\tt voxel-wise})$	0.94/0.06	1.00/0.00/0.00	2.47	0.84/0.15/0.01	6.75	
$\mathtt{NARM}(\alpha=0.15)$	0.96/0.04	0.98/0.02/0.00	2.35	1.00/0.00/0.00	3.31	
${\tt NARM} ({\tt no\ stopping\&rescaling})$	0.13/0.87	0.75/0.25/0.00	3.27	1.00/0.00/0.00	2.74	
$\boxed{ \text{PMARM}(c=0.05) }$	0.90/0.10	0.95/0.05/0.00	2.63	0.94/0.06/0.00	3.93	
$\mathtt{PMARM}(c=0.10)$	0.40/0.60	0.90/0.10/0.00	2.81	0.97/0.03/0.00	3.42	

We further explore the effectiveness of NARM extension with multiple b-values. We first create n=81 gradient directions equally spaced on the sphere, and we generate diffusion weighted measurements at  $b=1000s/mm^2$  on 41 out of 81 gradient directions (equally spaced), and diffusion weighted measurements at  $b=3000s/mm^2$  on the rest 40 gradient directions. We compare the performance of voxel-wise SN-lasso method on three datasets: the measurements at  $b=1000s/mm^2$  only, the measurements at  $b=3000s/mm^2$  only, and the measurements at both  $b=1000s/mm^2$  and  $b=3000s/mm^2$ . We also set the parameter  $\epsilon$  in the RSS-based  $\lambda$  selection (see Appendix 7.2 for more details) to be either  $10^{-3}$  or  $5\times 10^{-3}$  to investigate the effects of  $\lambda$  selection to the FOD estimation result, where larger  $\epsilon$  will lead to larger  $\lambda$  and thus sparser estimate. The performance of the NARM method applied on the diffusion weighted measurements at both  $b=1000s/mm^2$  and  $b=3000s/mm^2$  is also included to mimic our treatments in real data applications.

Several important findings can be concluded from Figure S.7, S.8, S.9 and Table S.6, S.7 in the Supplementary Material. First, the SN-lasso estimates on diffusion measurements at  $b = 1000\&3000s/mm^2$  is robust to the  $\lambda$  selection, with almost identical estimation results at  $\epsilon = 10^{-3}$  and  $5 \times 10^{-3}$ , whereas the SN-lasso estimates at  $b = 1000s/mm^2$  performs poorly at  $\epsilon = 5 \times 10^{-3}$  with no identified crossing fibers at all, and the SN-lasso estimates at  $b = 3000s/mm^2$  tends to over-smooth the zero fiber region at  $\epsilon = 10^{-3}$ . Second, even considering only the best case for each dataset, the SN-lasso estimates at  $b = 1000s/mm^2$  or

 $b=3000s/mm^2$  in terms of success rate, median angular error and mean Hellinger distance. This indicates the effectiveness of multiple b-value stacking in accurate fiber orientation estimation. In fact, sampling at a low b-value only would probably cause the loss of direction information in the FOD estimates and make the fiber tracking hard, while sampling at a high b-value only would probably bring in too much noise into FOD estimation. Third, the spatial smoothing procedure in NARM can further improve the recovery of FODs with much smaller median angular error in crossing fiber region. Its resulting fiber tracking plot is almost visually identical to the fiber tracking plot based on true FODs.

## 4.5 Summary

We have the following findings from 2D ROI simulation I & II and 3D ROI simulation. Firstly, the FOD estimation methods with spatial smoothing procedure outperform the voxel-wise SN-lasso method, especially in crossing fiber regions. Secondly, compared with PMARM (with best chosen stopping parameter c based on truth), the NARM method is able to produce more accurately orientated FOD estimates, and leads to more faithful recovery of fiber tracts. Thirdly, stopping rule is crucial for adaptive smoothing methods such as NARM and PMARM. Without stopping, the estimation can be overly smoothed, while stopping too early can lead to high variability. Our proposed stopping rule (including weight rescaling) for NARM is effective and robust to the hyper-parameter  $\alpha$ . In contrast, the stopping rule in PMARM is highly sensitive to the hyper-parameter c, making it hard to use in practice. Lastly, it is beneficial to combine observed diffusion measurements at multiple b-values, which would improve not only the accuracy of fiber direction estimation, but also the robustness of performance to the  $\lambda$  selection.

# 5 Real D-MRI data experiments: HCP

In this section, we implement our proposed method into a real D-MRI dataset obtained from the WU-Minn Human Connectome Project (HCP) database (https://www.humanconnectome.org/). The primary goal of HCP has been to map macroscopic human brain circuits and their relationship to behavior in a large population of healthy adults. The HCP dataset

includes high-resolution 3T MR scans from young healthy adult twins and non-twin siblings (ages 22-35) using four imaging modalities: structural images (T1w and T2w), resting-state fMRI (rfMRI), task-fMRI (tfMRI), and high angular resolution diffusion imaging (dMRI). See Van Essen et al. (2013) for more details of its scanner design, parameter setting and implementation. In the following, we analyze D-MRI dataset from one participant, a female in the age 31-35, to illustrate our methodology.

We use eddy-current-corrected diffusion images with diffusion weighted signals measured on a  $145 \times 174 \times 145$  3D grid (voxel side-length: x-1.25mm, y-1.25mm, z-1.25mm) along 270 distinct gradient directions, including 90 gradient directions under  $b = 1000s/mm^2$ , 90 gradient directions under  $b = 2000s/mm^2$  and 90 gradient directions under  $b = 3000s/mm^2$ . In addition, there are also 18  $b_0$  images and we estimate the  $b_0$  image intensity  $S_0$  and the Rician noise level  $\sigma$  based on them. The median signal-to-noise ratio  $S_0/\sigma$  across voxels is 20.7. We estimate the response function R by using the method proposed in Yan et al. (2018), where the estimated leading eigenvalue is  $1.3 \times 10^{-3}mm^2/s$  and the ratio between the leading and the minor eigenvalue is 6.1.

#### 5.1 ROI I

We focus on a  $15 \times 15 \times 15$  subregion (ROI I) of the D-MRI dataset, with x-slices 54-68, y-slices 118-132 and z-slices 61:75. This ROI contains the intersections of corpus callosum (CC), cingulum bundle (CB) and superior occipitofrontal fasciculus (SOF) according to the FSL Jülich Histological Atlas (Eickhoff et al. 2005, 2006, 2007). The left panel of Figure S.10(a) shows the fiber orientation colormap on the entire brain at z-slice 71, where the ROI is indicated by the white box. The fiber orientation colormap depicts the direction of principle eigenvector under single tensor model, where red stands for left-to-right direction, green stands for up-to-down direction and blue stands for into-to-out-of-page direction. The fiber orientation colormap is further modulated by the FA values such that it becomes darker as the FA value gets smaller. The rest plots in Figure S.10(a) are the zoomed-in version of the fiber orientation colormap, FA map and MD map on the ROI at z-slice 71. In the FA/MD maps, the color also becomes darker as the FA/MD value gets smaller. The details of FA/MD calculation are in Section S.2.1 of the Supplementary Material.

We apply the voxel-wise SN-lasso method to three distinct datasets: the diffusion measurements along 90 gradient directions at  $b = 1000s/mm^2$ , the diffusion measurements along 90 gradient directions at  $b = 3000s/mm^2$ , and the diffusion measurements along 270 gradient directions at  $b = 1000s/mm^2$ ,  $2000s/mm^2$  and  $3000s/mm^2$  (i.e., the entire set of measurements). We also apply the NARM method onto the entire set of measurements to demonstrate the effectiveness of our proposed spatial smoothing method. We set  $\gamma = 4$  in  $K_{\text{sim}}(u) = \exp(-\gamma u^2)$ . Here we focus on the ROI at z-slice 71 since this subregion contains several crossing fiber tracts as well as CSF as shown below.

Figure S.10(b) shows the images of FOD estimates on z-slice 71. We can see that all the methods produce satisfactory FOD estimates in the single fiber region, with clear peak directions consistent with the ones suggested by the fiber orientation colormap. However, the method performance differs quite a lot in the crossing fiber region. We take the bottom right part of this region as an example (indicated by the white box), where we have low FA values in the middle as well as low MD values. This is indeed a strong indication of crossing fibers rather than CSF since CSF is believed to have large MD values due to its fast water diffusion. From the zoomed-in subregion plots in Figure S.11, it can be seen that in the crossing fiber region, the SN-lasso at  $b = 1000s/mm^2$  leads to less pointy estimates with less direction information contained, whereas the SN-lasso at  $b = 3000s/mm^2$  tends to produce very noisy estimates without clear pattern. The SN-lasso estimates based on all three b-values outperform the previous two estimates in more coherent fiber crossings in this subregion. And by applying the NARM method, the FOD estimates are further improved with more clearly orientated fiber directions and less spurious fiber peaks. We also look into the top right corner of the region in Figure S.10, which is likely to be CSF due to small FA values and large MD values. The best FOD estimates to capture this isotropic structure is from the NARM method, where the largest number of isotropic fibers are identified in this subregion. In contrast, the FOD estimates without spatial smoothing procedure contain less isotropic fibers, and among them the SN-lasso estimates at  $b = 3000s/mm^2$  performs the worst, and the possible reason is that it may be hard to get rid of the noisy information from the diffusion measurements at  $b = 3000s/mm^2$  only.

Figure 4 and S.12 present the fiber tracking results at two different perspectives by

applying the deterministic tracking algorithm (Wong et al. 2016) to the extracted peaks from FOD estimates on the entire ROI. These tracking results reveal the fiber tracts in the atlas, where the red fiber bundle corresponds to CC, the bigger green bundle on the left corresponds to SOF and the smaller green bundle on the top right corresponds to CB. Among the tracking results based on four different estimates, the result based on the NARM estimates (Figure 4(d) and S.12(d)) shows the clearest crossings between the red fiber tracts and the green fiber tracts. Moreover, both the red and green fiber tracts in the result based on the NARM estimates are more tightly clustered, smoothly curved and parallel to each other than those in other results. Compared with the tracking results based on the SN-lasso estimates at  $b = 1000 s/mm^2$  or at  $b = 3000 s/mm^2$  only, the tracking result based on the SN-lasso estimates at all three b-values shows more coherent and less noisy fiber tracts, with a larger value of median fiber length at 5.84. In contrast, the SN-lasso estimates at  $b = 1000 s/mm^2$  leads to difficulties in fiber tracking due to its lack of direction information, thus the resulting fiber lengths have the lowest median value 4.30. Meanwhile, the SN-lasso estimates at  $b = 3000 s/mm^2$  involves too much noise, and we can see clearly from Figure S.12(b) that the tracking result contains spurious fiber tracts in the top right part of the ROI which is believed to be CSF according to the FA and MD maps. In conclusion, when comparing with the SN-lasso based on single b-value measurements, the SN-lasso based on multiple b-value measurements can produce more coherent and clear tracking result, and the NARM method in which spatial smoothing procedure is implemented can further improve the smoothness and parallelism of the tracking result to make it more biologically meaningful and interpretable.

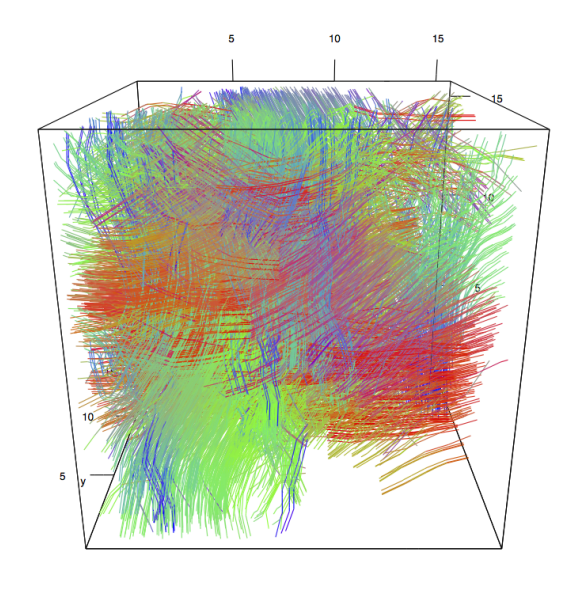
Figure 4: ROI I in HCP: Tracking results.

(a) SN-lasso(voxel-wise)(b = 1K)

(fiber number: 3556, fiber length: 4.30)

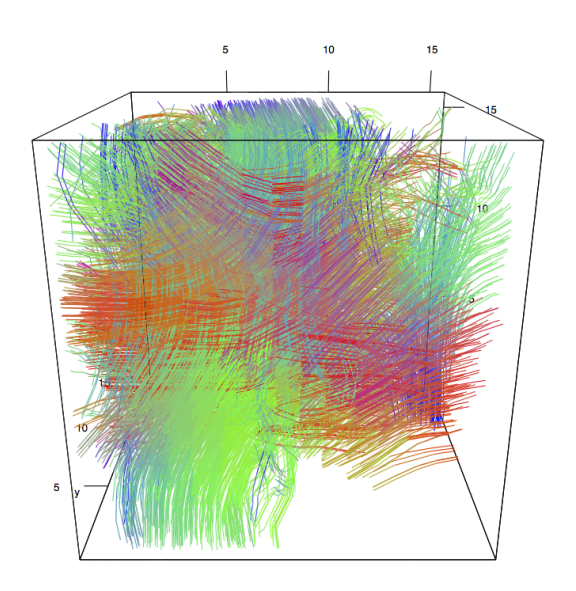
(b) SN-lasso(voxel-wise)(b = 3K)

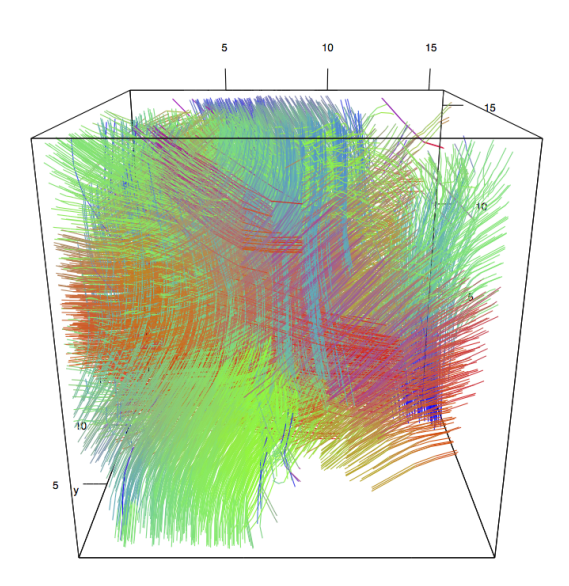
(fiber number: 5445, fiber length: 5.32)



(c) SN-lasso(voxel-wise)(b = 1K&2K&3K) (fiber number: 4596, fiber length: 5.84)

(d) NARM(b = 1K&2K&3K)(fiber number: 5007, fiber length: 6.80)





To further demonstrate the effectiveness of our proposed spatial smoothing method NARM, we also apply the voxel-wise SN-lasso method and the NARM method to D-MRI dataset in HCP retest data from the same participant. We use the FLIRT module in FSL to align the ROI I in test data to retest data, and it appears that the locations of ROI I in test data and retest data are almost identical, where we have x-slices 54-68, y-slices 118-132 and z-slices 61-75 in test data, and x-slices 54-68, y-slices 119-133 and z-slices 60-74 in retest data.

We also use a variety of numerical metrics to examine the consistency of FOD estimates in test and retest data by using the voxel-wise SN-lasso method and the NARM method respectively. Since test and retest data are obtained with independent errors, we believe that if the estimates in test and retest data are similar, they should be similar to the underlying truth. In other words, the FOD estimates should be more accurate if the estimates in test and retest data are more consistent. The numerical metrics we have used include: (1) The proportions of voxels where the numbers of detected fiber bundles match between test and retest data (number of voxels with a certain detected fiber number in both test and retest data, divided by number of voxels with this detected fiber number in either test or retest data), reported under "Matched" in the tables. (2) Among the "matched" voxels, the median angular difference between the identified fiber direction(s) in test and retest data, shown under "Diff." in the tables. (3) The mean and standard deviation (across all voxels in ROI) of the Hellinger distance between the estimated FODs in test and retest data. They are shown under "Mean H-dist." and "SD H-dist." in the tables. (4) Relative difference of numbers of connected fiber tracks across  $3 \times 3 \times 3$  subregions in ROI between test and retest data (for each pair of  $3 \times 3 \times 3 = 27$  subregions, relative difference of numbers of connected fiber tracks across the corresponding two subregions in the pair between test and retest data is calculated, and the mean of relative differences is reported). They are shown under "Mean Track Diff." in the tables.

Table 4: **HCP test-retest**: Success rate and angular error.

	0-Fiber	1-Fiber		2-Fiber		
Estimator	Co./Ov.	Co./Ov./Un.	Err.	Co./Ov./Un.	Err.	
SN-lasso(noiseless)	1.00/0.00	1.00/0.00/0.00	1.61	1.00/0.00/0.00	1.77	
${\tt SN-lasso}({\tt voxel-wise})$	0.94/0.06	1.00/0.00/0.00	2.47	0.84/0.15/0.01	6.75	
$\mathtt{NARM}(\alpha=0.15)$	0.96/0.04	0.98/0.02/0.00	2.35	1.00/0.00/0.00	3.31	
${\tt NARM} ({\tt no\ stopping\&rescaling})$	0.13/0.87	0.75/0.25/0.00	3.27	1.00/0.00/0.00	2.74	
$\mathtt{PMARM}(c=0.05)$	0.90/0.10	0.95/0.05/0.00	2.63	0.94/0.06/0.00	3.93	
$\mathtt{PMARM}(c=0.10)$	0.40/0.60	0.90/0.10/0.00	2.81	0.97/0.03/0.00	3.42	

Table 4 reports the quantitative summaries of the consistency of FOD estimates in test and retest data. We can see that the estimates by using NARM are more similar between test and retest data than the estimates by using voxel-wise SN-lasso, according to higher matching rate and lower median angular difference in zero-fiber, one-fiber and two-fiber regions, as well as lower mean Hellinger distance. Moreover, the fiber tracks obtained from the deterministic tracking algorithm shows more consistent pattern between test and retest data in NARM than voxel-wise SN-lasso, where the mean relative difference of numbers of connected fiber tracks across subregions is smaller in NARM. As previously pointed out, the more consistent the FOD estimates in test and retest data are, the more close these estimates are to the underlying truth, and thus the more accurate the FOD estimation method is. Therefore, the NARM method has outperformed the voxel-wise SN-lasso method in this real data experiment.

#### 5.2 ROI II

The second subregion (ROI II) we are going to explore in the same HCP dataset is a  $20 \times 20 \times 20$  region with x-slices 56-75, y-slices 86-105 and z-slices 66-85. According to the FSL Jülich Histological Atlas, this region contains the intersections of four tracts including corpus callosum (CC), cingulum bundle (CB), superior occipitofrontal fasciculus (SOF) and corticospinal tract (CT). The ROI at z-slice 82 is shown by the white box in the left

panel of Figure S.13(a) and its corresponding zoomed-in fiber orientation colormap, FA map and MD map are also shown in Figure S.13(a).

We present the FOD estimates on z-slice 82 in Figure S.13(b). According to the FA and MD maps in Figure S.13(a), the middle part of the region (highlighted by the white box) is very likely to contain crossing fibers due to both small FA and MD values. This is corroborated by the NARM estimates shown in the zoomed-in subregion plots in Figure S.14, where they clearly capture the crossing between a fiber in the left-to-right direction and a fiber in the up-to-down direction, as indicated by the colormap as well. The other voxel-wise SN-lasso estimates again contain many spurious peaks and do not show clear directionality. The right part of the region in Figure S.13 is probably CSF which shows large MD values and small FA values. Among all the four FOD estimates, the NARM estimates depict the isotropic region the best where FODs in most part of this subregion are estimated as isotropic. On the contrary, the SN-lasso estimates at  $b = 3000s/mm^2$  perform the worst in identifying isotropic voxels.

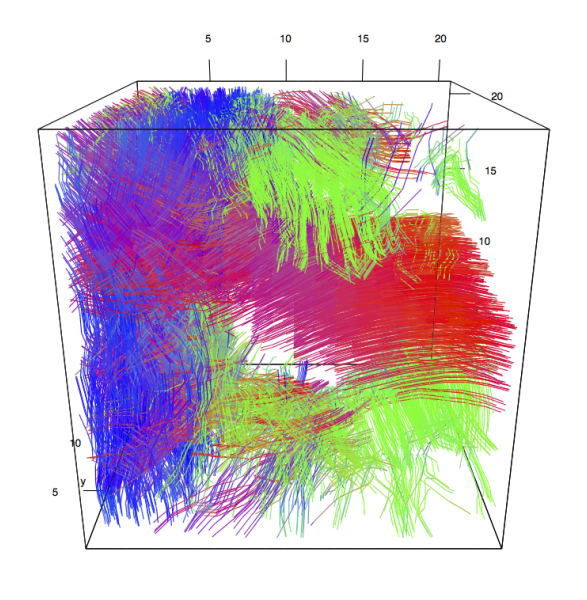
The reconstructed fiber tracks are presented in Figure 5 and S.15 at two different perspectives. All the four fiber tracks in the atlas are clearly shown in the tracking results, where the blue tracts correspond to CT, the red tracts correspond to CC, the green tracts in the top correspond to CB and the green tracts in the bottom correspond to SOF. Similar to our previous findings, the NARM estimates also produce the smoothest and most coherent trajectories, whereas the SN-lasso estimates at  $b = 1000s/mm^2$  struggles in finding appropriate fiber directions and results in the smallest median fiber length, and the SN-lasso estimates at  $b = 3000s/mm^2$  generate too many noisy tracts in the top right corner of the ROI.

Figure 5: ROI II in HCP: Tracking results.

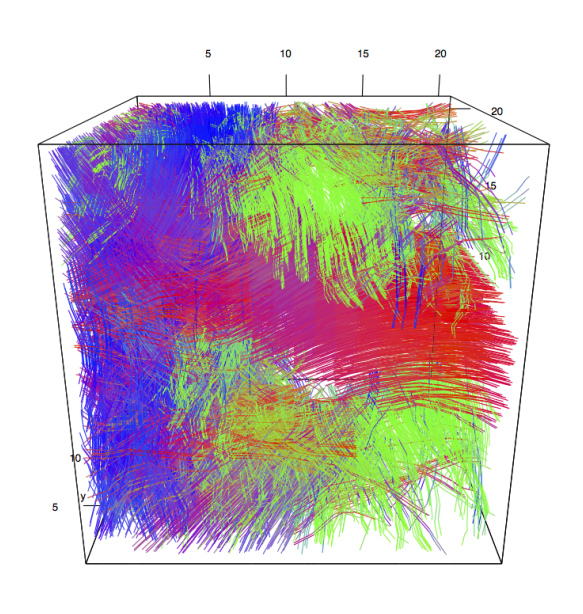
(a) SN-lasso(voxel-wise)(b = 1K)

(fiber number: 7933, fiber length: 4.21)

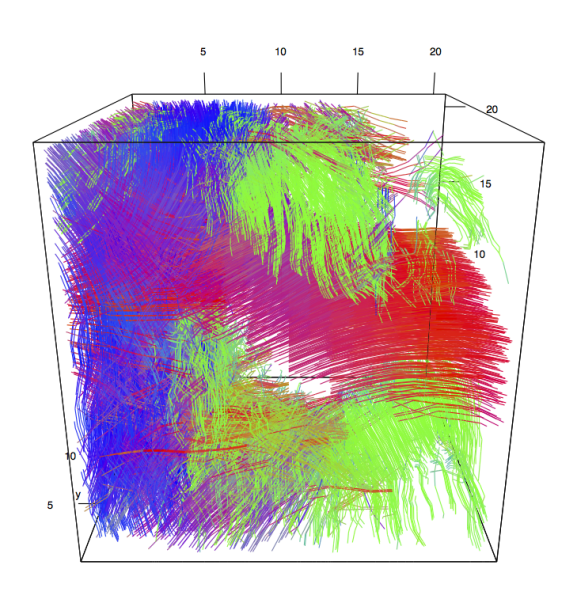
(b) SN-lasso(voxel-wise)(b = 3K) (fiber number: 12249, fiber length: 6.13)

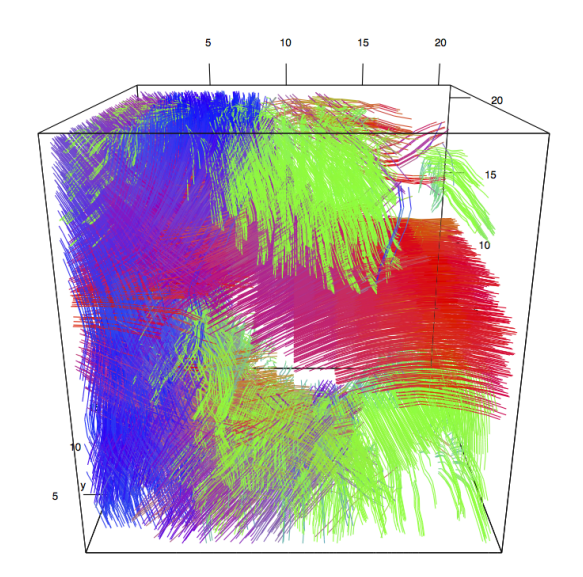


(c) SN-lasso(voxel-wise)(b = 1K&2K&3K) (fiber number: 9374, fiber length: 6.43)



 $\label{eq:definition} \mbox{(d) NARM}(b=1K\&2K\&3K)$  (fiber number: 9075, fiber length: 7.65)





## 6 Conclusions

In this paper, we have proposed a Nearest-neighbor Adaptive Regression Model (NARM) to adaptively estimate the FODs across all voxels using D-MRI data. NARM is able to incorporate spatial constraint in D-MRI data for fiber reconstruction by adaptively borrowing information from neighboring voxels. NARM has improved the existing PMARM method (Rao et al. 2016) in three major aspects: the Hellinger distance in FOD similarity measurement which makes FODs with different peak orientations more distinguishable, the weight rescaling process which well handles the extreme cases in smoothing, and the stopping rule based on the minimum nearest-neighbor distance which is easy to implement in practice and is effective in preventing over-smoothing. Moreover, NARM is further extended to the cases where diffusion measurements are sampled with multiple b-values.

Experimental results on synthetic data demonstrate that NARM results in better FOD reconstruction than the voxel-wise SN-lasso method and the existing PMARM method, where it leads to more accurate and less noisy fiber orientation detection, and more coherent and smoother fiber tracking result. In experiments on real 3T D-MRI datasets, the NARM estimates lead to clearer crossing fiber regions and more biologically sensible and interpretable tractography results than the voxel-wise SN-lasso method. Moreover, the SN-lasso estimates based on diffusion measurements at multiple b-values perform better than those at single b-value in terms of the coherence and noise level of fiber tracts. Therefore, the NARM estimates based on diffusion measurements at multiple b-values would provide more useful information on brain connectivity and lead to better understanding of brain structure and functionality.

One direction for future research is to further improve the similarity measure between FODs in weight calculation. The Hellinger distance we are currently using is able to better identify the difference between peak values of FODs than the  $l_2$  distance. However, the Hellinger distance is not very sensitive to the peak orientation shift of FODs since it is not very aware of the peak location. Some location-aware distances between density functions can be explored in the future, for example, the earth-mover distance. However, the computational efficiency is a big issue since the computation cost of the earth-mover distance is much expensive than that of the Hellinger distance.

## 7 Appendix

#### 7.1 ADMM algorithm in SN-lasso

We first simplify the notation in the optimization problem (4). Let

$$oldsymbol{eta} = oldsymbol{eta}(oldsymbol{v}) \in \mathbb{R}^p, \; oldsymbol{y} = oldsymbol{y}(oldsymbol{v}) \in \mathbb{R}^n, \; oldsymbol{X} = oldsymbol{\Phi} oldsymbol{R} oldsymbol{C} \in \mathbb{R}^{n imes p}, \; oldsymbol{C} = ilde{oldsymbol{\Phi}} oldsymbol{C} \in \mathbb{R}^{l imes p}.$$

Then (4) can be rewritten as

minimize 
$$\frac{1}{2}||\boldsymbol{y} - \boldsymbol{X}\boldsymbol{\beta}||_2^2 + \lambda||\boldsymbol{\beta}||_1$$
, subject to  $\boldsymbol{C}\boldsymbol{\beta} \succ \boldsymbol{0}$ .

To solve this optimization problem using ADMM algorithm, we notice that it can be further written as

minimize 
$$\frac{1}{2}||\boldsymbol{y} - \boldsymbol{X}\boldsymbol{\beta}||_2^2 + \lambda||\boldsymbol{\gamma}||_1 + I_+(\boldsymbol{\eta}),$$
  
subject to  $\boldsymbol{\beta} - \boldsymbol{\gamma} = \boldsymbol{0}, \ \boldsymbol{C}\boldsymbol{\beta} - \boldsymbol{\eta} = \boldsymbol{0},$ 

where  $\gamma \in \mathbb{R}^p$ ,  $\eta \in \mathbb{R}^l$ ,  $I_+(\eta) = 0$  when  $\eta \geq 0$  (elementwise) and  $I_+(\eta) = \infty$  otherwise.

The scaled augmented Lagrangian is

$$L_{\rho}(\boldsymbol{\beta}, \boldsymbol{\gamma}, \boldsymbol{\eta}, \boldsymbol{u}, \boldsymbol{t}) = \frac{1}{2}||\boldsymbol{y} - \boldsymbol{X}\boldsymbol{\beta}||_{2}^{2} + \lambda||\boldsymbol{\gamma}||_{1} + I_{+}(\boldsymbol{\eta}) + \frac{\rho}{2}||\boldsymbol{\beta} - \boldsymbol{\gamma} + \boldsymbol{u}||_{2}^{2} + \frac{\rho}{2}||\boldsymbol{C}\boldsymbol{\beta} - \boldsymbol{\eta} + \boldsymbol{t}||_{2}^{2},$$

where  $\boldsymbol{u} \in \mathbb{R}^p$  and  $\boldsymbol{t} \in \mathbb{R}^l$  are dual variables.

The ADMM algorithm for SN-lasso is presented as follows. We first initialize  $\gamma = 0$ ,  $\eta = 0$ , u = 0, t = 0. We also need to specify  $\rho(>0)$ , which in practice is recommended to be  $\approx \lambda$  (Wahlberg et al. 2012). For step  $s = 1, 2, \ldots$  until convergence:

(i)  $\beta$ -minimization.

$$\beta^{s} = \arg\min_{\beta} \frac{1}{2} ||\boldsymbol{y} - \boldsymbol{X}\beta||_{2}^{2} + \frac{\rho}{2} ||\boldsymbol{\beta} - \boldsymbol{\gamma}^{s-1} + \boldsymbol{u}^{s-1}||_{2}^{2} + \frac{\rho}{2} ||\boldsymbol{C}\beta - \boldsymbol{\eta}^{s-1} + \boldsymbol{t}^{s-1}||_{2}^{2}$$

$$= (\boldsymbol{X}^{T}\boldsymbol{X} + \rho \boldsymbol{I}_{p} + \rho \boldsymbol{C}^{T}\boldsymbol{C})^{-1} (\boldsymbol{X}^{T}\boldsymbol{y} + \rho(\boldsymbol{\gamma}^{s-1} - \boldsymbol{u}^{s-1}) + \rho \boldsymbol{C}^{T}(\boldsymbol{\eta}^{s-1} - \boldsymbol{t}^{s-1})).$$

Cholesky decomposition can be used for the matrix inversion.

(ii)  $\gamma/\eta$ -minimization.

$$\begin{split} \boldsymbol{\gamma}^s &= \arg\min_{\boldsymbol{\gamma}} \frac{\rho}{2} ||\boldsymbol{\beta}^s - \boldsymbol{\gamma} + \boldsymbol{u}^{s-1}||_2^2 + \lambda ||\boldsymbol{\gamma}||_1 = S_{\lambda/\rho} (\boldsymbol{\beta}^s + \boldsymbol{u}^{s-1}), \\ \text{where } S_{\lambda/\rho} (\boldsymbol{\beta}^s + \boldsymbol{u}^{s-1})_i = (|\beta_i^s + u_i^{s-1}| - \frac{\lambda}{\rho})_+ \mathrm{sign}(\beta_i^s + u_i^{s-1}). \\ \boldsymbol{\eta}^s &= \arg\min_{\boldsymbol{\eta}} \frac{\rho}{2} ||\boldsymbol{C}\boldsymbol{\beta}^s - \boldsymbol{\eta} + \boldsymbol{t}^{s-1}||_2^2 + I_+(\boldsymbol{\eta}) = \max\left\{\boldsymbol{0}, \; \boldsymbol{C}\boldsymbol{\beta}^s + \boldsymbol{t}^{s-1}\right\}, \end{split}$$

where the maximum is taken elementwisely.

(iii) dual-update.

$$\boldsymbol{u}^s = \boldsymbol{u}^{s-1} + \boldsymbol{\beta}^s - \boldsymbol{\gamma}^s, \quad \boldsymbol{t}^s = \boldsymbol{t}^{s-1} + \boldsymbol{C}\boldsymbol{\beta}^s - \boldsymbol{\eta}^s.$$

#### Over-relaxation

Over-relaxation can accelerate convergence. We replace  $\boldsymbol{\beta}^s$  with  $\alpha \boldsymbol{\beta}^s + (1-\alpha)\boldsymbol{\gamma}^{s-1}$ , and replace  $\boldsymbol{C}\boldsymbol{\beta}^s$  with  $\alpha \boldsymbol{C}\boldsymbol{\beta}^s + (1-\alpha)\boldsymbol{\eta}^{s-1}$  in  $\boldsymbol{\gamma}/\boldsymbol{\eta}$ -minimization and dual-update, where the relaxation parameter  $\alpha$  is set to be 1.5.

#### Stopping criterion

The norm of the primal residual at step s is  $||\boldsymbol{r}^s||_2 = (||\boldsymbol{\beta}^s - \boldsymbol{\gamma}^s||_2^2 + ||\boldsymbol{C}\boldsymbol{\beta}^s - \boldsymbol{\eta}^s||_2^2)^{\frac{1}{2}}$ , and the norm of the dual residual at step s is  $||\boldsymbol{d}^s||_2 = \rho||(\boldsymbol{\gamma}^s - \boldsymbol{\gamma}^{s-1}) + \boldsymbol{C}^T (\boldsymbol{\eta}^s - \boldsymbol{\eta}^{s-1})||_2$ . Define the feasibility tolerance for the primal as  $\epsilon^{\text{pri}} = \epsilon^{\text{abs}} \sqrt{p+l} + \epsilon^{\text{rel}} \max\{(||\boldsymbol{\beta}^s||_2^2 + ||\boldsymbol{C}\boldsymbol{\beta}^s||_2^2)^{\frac{1}{2}},$   $(||\boldsymbol{\gamma}^s||_2^2 + ||\boldsymbol{\eta}^s||_2^2)^{\frac{1}{2}}\}$ , and the feasibility tolerance for the dual as  $\epsilon^{\text{dual}} = \epsilon^{\text{abs}} \sqrt{p} + \epsilon^{\text{rel}} \rho ||\boldsymbol{u}^s + \boldsymbol{C}^T \boldsymbol{t}^s||_2$ . Here  $\epsilon^{\text{abs}}$  is the absolute tolerance and in practice is often set as  $10^{-5}$  or  $10^{-4}$ , and  $\epsilon^{\text{rel}}$  is the relative tolerance and in practice is often set as  $10^{-3}$  or  $10^{-2}$ . The stopping criterion is that the algorithm stops if and only if  $||\boldsymbol{r}^s||_2 \leq \epsilon^{\text{pri}}$  and  $||\boldsymbol{d}^s||_2 \leq \epsilon^{\text{dual}}$ .

## 7.2 $\lambda$ selection for $l_1$ penalty in SN-lasso

We start from a sequence of  $\lambda$ 's with decreasing values  $\lambda_1 > \ldots > \lambda_K$ , fit the model sequentially and calculate their corresponding residual sum of squares  $RSS_k$ ,  $k = 1, \ldots, K$ . We then obtain the relative change of  $RSS_k$  by calculating  $\delta_k := |(\log RSS_k - \log RSS_{k-1})/(\log \lambda_k - \log \lambda_{k-1})|$ ,  $k = 2, \ldots, K$ . We select the optimal value of  $\lambda$  from the decreasing  $\lambda$ 's

once the average of T consecutive relative changes is smaller than a pre-specified threshold  $\epsilon$ , i.e.,  $\lambda_{opt} := \lambda_{k^*}$ , where  $k^* = \min\{T + 1 \le k \le K : \frac{1}{T} \sum_{l=0}^{T-1} \delta_{k-l} < \epsilon\}$ .

In simulation studies, we set the sequence of  $\lambda$ 's as K=100 equally spaced grid points on the log-scale on  $10^0 \sim 10^{-5}$ , and  $T=5\% \times 100=5$ . Unless otherwise specified, the threshold  $\epsilon$  is set to be  $10^{-3}$  in  $b=1000s/mm^2$  cases and  $5\times 10^{-3}$  in  $b=3000s/mm^2$  cases. In D-MRI real data experiments using HCP data, we set the sequence of  $\lambda$ 's as K=120 equally spaced grid points on the log-scale on  $10^{0.5} \sim 10^{-5}$ ,  $T=5\% \times 120=6$ , and the threshold  $\epsilon$  to be  $3\times 10^{-3}$ .

## References

- Basser, P. J. & Jones, D. K. (2002), 'Diffusion-tensor mri: theory, experimental design and data analysis—a technical review', *NMR in Biomedicine* **15**(7-8), 456–467.
- Basser, P. J., Mattiello, J. & LeBihan, D. (1994), 'Mr diffusion tensor spectroscopy and imaging', *Biophysical journal* **66**(1), 259–267.
- Basser, P. J., Pajevic, S., Pierpaoli, C., Duda, J. & Aldroubi, A. (2000), 'In vivo fiber tractography using dt-mri data', *Magnetic resonance in medicine* **44**(4), 625–632.
- Becker, S., Tabelow, K., Mohammadi, S., Weiskopf, N. & Polzehl, J. (2014), 'Adaptive smoothing of multi-shell diffusion weighted magnetic resonance data by mspoas', *NeuroImage* **95**, 90–105.
- Becker, S., Tabelow, K., Voss, H. U., Anwander, A., Heidemann, R. M. & Polzehl, J. (2012), 'Position-orientation adaptive smoothing of diffusion weighted magnetic resonance data (poas)', *Medical image analysis* **16**(6), 1142–1155.
- Boyd, S., Parikh, N., Chu, E., Peleato, B., Eckstein, J. et al. (2011), 'Distributed optimization and statistical learning via the alternating direction method of multipliers', Foundations and Trends® in Machine learning 3(1), 1–122.
- Descoteaux, M., Angelino, E., Fitzgibbons, S. & Deriche, R. (2007), 'Regularized, fast, and robust analytical q-ball imaging', *Magnetic resonance in medicine* **58**(3), 497–510.

- Descoteaux, M., Deriche, R., Knosche, T. R. & Anwander, A. (2009), 'Deterministic and probabilistic tractography based on complex fibre orientation distributions', *IEEE transactions on medical imaging* **28**(2), 269–286.
- Eickhoff, S. B., Heim, S., Zilles, K. & Amunts, K. (2006), 'Testing anatomically specified hypotheses in functional imaging using cytoarchitectonic maps', *Neuroimage* **32**(2), 570–582.
- Eickhoff, S. B., Paus, T., Caspers, S., Grosbras, M.-H., Evans, A. C., Zilles, K. & Amunts, K. (2007), 'Assignment of functional activations to probabilistic cytoarchitectonic areas revisited', *Neuroimage* **36**(3), 511–521.
- Eickhoff, S. B., Stephan, K. E., Mohlberg, H., Grefkes, C., Fink, G. R., Amunts, K. & Zilles, K. (2005), 'A new spm toolbox for combining probabilistic cytoarchitectonic maps and functional imaging data', *Neuroimage* **25**(4), 1325–1335.
- Fan, J. & Gijbels, I. (1996), Local polynomial modelling and its applications: monographs on statistics and applied probability 66, Vol. 66, CRC Press.
- Gudbjartsson, H. & Patz, S. (1995), 'The rician distribution of noisy mri data', *Magnetic resonance in medicine* **34**(6), 910–914.
- Hahn, K. R., Prigarin, S., Heim, S. & Hasan, K. (2006), Random noise in diffusion tensor imaging, its destructive impact and some corrections, *in* 'Visualization and Processing of Tensor Fields', Springer, pp. 107–119.
- Jensen, J. H., Glenn, G. R. & Helpern, J. A. (2016), 'Fiber ball imaging', *Neuroimage* **124**, 824–833.
- Le Bihan, D. & Warach, S. J. (1995), 'Diffusion and perfusion magnetic resonance imaging: Applications to functional mri.'.
- Li, Y., Zhu, H., Shen, D., Lin, W., Gilmore, J. H. & Ibrahim, J. G. (2011), 'Multiscale adaptive regression models for neuroimaging data', *Journal of the Royal Statistical Society:*Series B (Statistical Methodology) 73(4), 559–578.

- Liu, M., Vemuri, B. C. & Deriche, R. (2013), 'A robust variational approach for simultaneous smoothing and estimation of dti', *NeuroImage* **67**, 33–41.
- Mori, S. (2007), Introduction to diffusion tensor imaging, Elsevier.
- Narcowich, F. J., Petrushev, P. & Ward, J. D. (2006a), 'Localized tight frames on spheres', SIAM Journal on Mathematical Analysis 38(2), 574–594.
- Narcowich, F., Petrushev, P. & Ward, J. (2006b), 'Decomposition of besov and triebel–lizorkin spaces on the sphere', *Journal of Functional Analysis* **238**(2), 530–564.
- Polzehl, J. & Spokoiny, V. (2006), 'Propagation-separation approach for local likelihood estimation', *Probability Theory and Related Fields* **135**(3), 335–362.
- Polzehl, J. & Spokoiny, V. G. (2000), 'Adaptive weights smoothing with applications to image restoration', *Journal of the Royal Statistical Society: Series B (Statistical Methodology)* **62**(2), 335–354.
- Raj, A., Hess, C. & Mukherjee, P. (2011), 'Spatial hardi: improved visualization of complex white matter architecture with bayesian spatial regularization', *Neuroimage* **54**(1), 396–409.
- Rao, S., Ibrahim, J. G., Cheng, J., Yap, P.-T. & Zhu, H. (2016), 'Sr-hardi: Spatially regularizing high angular resolution diffusion imaging', *Journal of Computational and Graphical Statistics* **25**(4), 1195–1211.
- Sporns, O. (2010), Networks of the Brain, MIT press.
- Tabelow, K., Polzehl, J., Spokoiny, V. & Voss, H. U. (2008), 'Diffusion tensor imaging: structural adaptive smoothing', *NeuroImage* **39**(4), 1763–1773.
- Tournier, J.-D., Calamante, F. & Connelly, A. (2007), 'Robust determination of the fibre orientation distribution in diffusion mri: non-negativity constrained super-resolved spherical deconvolution', *Neuroimage* **35**(4), 1459–1472.

- Tournier, J.-D., Calamante, F., Gadian, D. G. & Connelly, A. (2004), 'Direct estimation of the fiber orientation density function from diffusion-weighted mri data using spherical deconvolution', *NeuroImage* **23**(3), 1176–1185.
- Tuch, D. S. (2004), 'Q-ball imaging', Magnetic resonance in medicine 52(6), 1358–1372.
- Tuch, D. S., Reese, T. G., Wiegell, M. R., Makris, N., Belliveau, J. W. & Wedeen, V. J. (2002), 'High angular resolution diffusion imaging reveals intravoxel white matter fiber heterogeneity', *Magnetic resonance in medicine* **48**(4), 577–582.
- Van Essen, D. C., Smith, S. M., Barch, D. M., Behrens, T. E., Yacoub, E., Ugurbil, K., Consortium, W.-M. H. et al. (2013), 'The wu-minn human connectome project: an overview', Neuroimage 80, 62-79.
- Wahlberg, B., Boyd, S., Annergren, M. & Wang, Y. (2012), 'An admm algorithm for a class of total variation regularized estimation problems', *IFAC Proceedings Volumes* **45**(16), 83–88.
- Wong, R. K., Lee, T. C., Paul, D. & Peng, J. (2016), 'Fiber direction estimation, smoothing and tracking in diffusion mri', *The annals of applied statistics* **10**(3), 1137.
- Yan, H., Carmichael, O., Paul, D. & Peng, J. (2018), 'Estimating fiber orientation distribution from diffusion mri with spherical needlets', *Medical image analysis* **46**, 57–72.
- Yu, T. & Li, P. (2013), 'Spatial shrinkage estimation of diffusion tensors on diffusion-weighted imaging data', *Journal of the American Statistical Association* **108**(503), 864–875.

# Estimating Spatially-Smoothed Fiber Orientation Distribution SUPPLEMENTARY MATERIAL

For figures in the supplementary material, check out https://github.com/jie108/FOD\_Narm\_codes/blob/master/narm\_arxiv.pdf.

# S.1 Synthetic experiments: additional details

## S.1.1 2D ROI simulation I

Table S.1: **2D ROI simulation I**: Hellinger distance.

	True F	ODs	Noiseless estimates		
Estimator	Mean H-dist.	SD H-dist.	Mean H-dist.	SD H-dist.	
SN-lasso(noiseless)	0.446	0.047	-	-	
${\tt SN-lasso}({\tt voxel-wise})$	0.498	0.053	0.225	0.128	
$\mathtt{NARM}(\alpha=0.10)$	0.470	0.038	0.179	0.075	
$\mathtt{NARM}(\alpha=0.15)$	0.470	0.038	0.182	0.076	
$\mathtt{NARM}(\alpha=0.20)$	0.470	0.038	0.180	0.076	
NARM(no stopping&rescaling)	0.509	0.054	0.329	0.103	
NARM(no stopping)	0.510	0.054	0.325	0.115	
$\mathtt{NARM}(\mathtt{no}\ \mathtt{rescaling})$	0.470	0.039	0.181	0.077	
$\mathtt{NARM}(\chi^2\text{-stopping},c=3)$	0.471	0.043	0.203	0.086	
$\mathtt{NARM}(\chi^2\text{-stopping},c=4)$	0.473	0.043	0.210	0.094	
$\mathtt{PMARM}(c=0.15)$	0.476	0.043	0.220	0.103	
$\mathtt{PMARM}(c=0.20)$	0.477	0.048	0.225	0.110	
$\mathtt{PMARM}(c=0.25)$	0.478	0.048	0.230	0.112	

## S.1.2 2D ROI simulation II

Table S.2: **2D ROI simulation II**: Hellinger distance.

	True F	ODs	Noiseless estimates		
Estimator	Mean H-dist.	SD H-dist.	Mean H-dist.	SD H-dist.	
SN-lasso(noiseless)	0.357	0.194	-	-	
${\tt SN-lasso}({\tt voxel-wise})$	0.404	0.202	0.169	0.147	
$\texttt{NARM}(\alpha=0.10)$	0.380	0.200	0.135	0.113	
$\mathtt{NARM}(\alpha=0.15)$	0.380	0.201	0.138	0.116	
$\mathtt{NARM}(\alpha=0.20)$	0.380	0.201	0.138	0.117	
NARM(no stopping&rescaling)	0.542	0.078	0.418	0.154	
NARM(no stopping)	0.449	0.201	0.320	0.187	
$\mathtt{NARM}(\mathtt{no}\ \mathtt{rescaling})$	0.380	0.201	0.136	0.116	
$\mathtt{NARM}(\chi^2\text{-stopping},c=2)$	0.414	0.189	0.189	0.157	
$\mathtt{NARM}(\chi^2\text{-stopping},c=3)$	0.413	0.190	0.194	0.158	
$\mathtt{NARM}(\chi^2\text{-stopping},c=4)$	0.415	0.191	0.200	0.162	
	0.385	0.203	0.167	0.131	
$\mathtt{PMARM}(c=0.10)$	0.377	0.204	0.268	0.195	

## S.1.3 3D ROI simulation at $b = 1000s/mm^2$

Figure S.1: **3D ROI simulation**: True FOD images and fiber tracts.

(a) True FOD images on 5 z-slices

z-slice 1 z-slice 2 z-slice 3

z-slice 4 z-slice 5

(b) Fiber tracts based on true FODs

perspective 1 perspective 2 perspective 3

Table S.3: **3D ROI simulation**: Hellinger distance.

	True F	ODs	Noiseless estimates		
Estimator	Mean H-dist. SD H-dist.		Mean H-dist.	SD H-dist.	
SN-lasso(noiseless)	0.379	0.135	-	-	
${\tt SN-lasso}({\tt voxel-wise})$	0.450	0.165	0.234	0.171	
${\tt NARM}(\alpha=0.15)$	0.402	0.143	0.144	0.099	
${\tt NARM} ({\tt no\ stopping\&rescaling})$	0.457	0.096	0.252	0.161	
$\boxed{ \text{PMARM}(c=0.05) }$	0.422	0.151	0.201	0.140	
$\mathtt{PMARM}(c=0.10)$	0.445	0.117	0.225	0.151	

Figure S.2: **3D ROI simulation**: FOD estimates on z-slice 4. (a) True FODs in SH basis; (b) SN-lasso (voxel-wise) estimates; (c) NARM ( $\alpha = 0.15$ ) estimates; (d) NARM (no stopping&rescaling) estimates; (e) PMARM (c = 0.05) estimates; (f) PMARM (c = 0.10) estimates.

- (a) True FODs
- (b) SN-lasso (voxel-wise)
- (c) NARM( $\alpha = 0.15$ )
- (d) NARM(no stopping&rescaling)
- (e) PMARM(c=0.05)
- (f) PMARM(c=0.10)

Figure S.3: **3D ROI simulation**: Tracking results. (a) True FODs in SH basis; (b) SN-lasso (voxel-wise) estimates; (c) NARM ( $\alpha = 0.15$ ) estimates; (d) NARM (no stopping&rescaling) estimates; (e) PMARM (c = 0.05) estimates; (f) PMARM (c = 0.10) estimates.

(a) True FODs

(b) SN-lasso (voxel-wise)

(fiber number: 451, fiber length: 5.59)

- (fiber number: 392, fiber length: 4.11)
- (c) NARM( $\alpha = 0.15$ )
- (d) NARM(no stopping&rescaling)

(fiber number: 420, fiber length: 4.63)

(fiber number: 489, fiber length: 5.43)

(e) PMARM(c=0.05)

(f) PMARM(c=0.10)

(fiber number: 398, fiber length: 4.23)

(fiber number: 440, fiber length: 4.75)

## S.1.4 3D ROI simulation at $b = 3000s/mm^2$

Figure S.4: **3D ROI simulation** ( $b = 3000s/mm^2$ ): FOD estimates on z-slice 2. (a) True FODs; (b) SN-lasso (voxel-wise) estimates; (c) NARM ( $\alpha = 0.15$ ) estimates; (d) NARM (no stopping&rescaling) estimates; (e) PMARM (c = 0.05) estimates; (f) PMARM (c = 0.10) estimates.

- (a) True FODs (b) SN-lasso (voxel-wise) (c) NARM( $\alpha=0.15$ ) (d) NARM(no stopping&rescaling)
- (e) PMARM(c=0.05) (f) PMARM(c=0.10)

Figure S.5: **3D ROI simulation** ( $b = 3000s/mm^2$ ): FOD estimates on z-slice 4. (a) True FODs; (b) SN-lasso (voxel-wise) estimates; (c) NARM ( $\alpha = 0.15$ ) estimates; (d) NARM (no stopping&rescaling) estimates; (e) PMARM (c = 0.05) estimates; (f) PMARM (c = 0.10) estimates.

- (a) True FODs (b) SN-lasso (voxel-wise)
- (c)  $NARM(\alpha = 0.15)$  (d) NARM(no stopping&rescaling)
- $(e) \ \mathtt{PMARM}(c{=}0.05) \qquad \qquad (f) \ \mathtt{PMARM}(c{=}0.10)$

Figure S.6: **3D ROI simulation** ( $b = 3000s/mm^2$ ): Tracking results. (a) True FODs; (b) SN-lasso (voxel-wise) estimates; (c) NARM ( $\alpha = 0.15$ ) estimates; (d) NARM (no stopping&rescaling) estimates; (e) PMARM (c = 0.05) estimates; (f) PMARM (c = 0.10) estimates.

- (a) True FODs (b) SN-lasso (voxel-wise)
- (fiber number: 451, fiber length: 5.59) (fiber number: 430, fiber length: 4.68)
  - (c)  ${\tt NARM}(\alpha=0.15)$  (d)  ${\tt NARM}({\tt no\ stopping\&rescaling})$
- (fiber number: 439, fiber length: 4.90) (fiber number: 490, fiber length: 5.64)
  - (e) PMARM(c=0.05) (f) PMARM(c=0.10)
- (fiber number: 444, fiber length: 4.99) (fiber number: 488, fiber length: 5.65)

Table S.4: **3D ROI simulation** ( $b = 3000 s/mm^2$ ): Success rate and angular error.

	0-Fiber	1-Fiber		2-Fiber	
Estimator	Co./Ov.	Co./Ov./Un.	Err.	Co./Ov./Un.	Err.
SN-lasso(noiseless)	1.00/0.00	1.00/0.00/0.00	1.60	1.00/0.00/0.00	1.68
${\tt SN-lasso}({\tt voxel-wise})$	0.92/0.08	1.00/0.00/0.00	1.96	0.94/0.06/0.00	3.35
$\mathtt{NARM}(\alpha=0.15)$	0.98/0.02	0.97/0.03/0.00	1.82	1.00/0.00/0.00	2.42
${\tt NARM} ({\tt no\ stopping\&rescaling})$	0.27/0.73	0.79/0.21/0.00	2.62	1.00/0.00/0.00	2.29
$\mathtt{PMARM}(c=0.05)$	0.88/0.12	0.93/0.07/0.00	1.95	0.99/0.01/0.00	2.22
$\mathtt{PMARM}(c=0.10)$	0.31/0.69	0.85/0.15/0.00	2.13	1.00/0.00/0.00	2.28

Table S.5: **3D ROI simulation** ( $b = 3000s/mm^2$ ): Hellinger distance.

	True F	ODs	Noiseless estimates		
Estimator	Mean H-dist. SD H-dist.		Mean H-dist.	SD H-dist.	
SN-lasso(noiseless)	0.373	0.134	-	-	
${\tt SN-lasso}({\tt voxel-wise})$	0.398	0.137	0.160	0.102	
$\mathtt{NARM}(\alpha=0.15)$	0.382	0.135	0.114	0.077	
${\tt NARM} ({\tt no\ stopping\&rescaling})$	0.438	0.111	0.208	0.167	
$\mathtt{PMARM}(c=0.05)$	0.387	0.131	0.139	0.101	
$\mathtt{PMARM}(c=0.10)$	0.429	0.109	0.191	0.157	

## S.1.5 3D ROI simulation for multiple b-values

Figure S.7: **3D ROI simulation** (b = 1K, 3K, 1K&3K): FOD estimates on z-slice 2.

$$\epsilon=10^{-3} \qquad \qquad \epsilon=5\times 10^{-3}$$
 
$$\mathrm{SN-lasso}(b=1K) \qquad \mathrm{SN-lasso}(b=1K)$$
 
$$\mathrm{SN-lasso}(b=3K) \qquad \mathrm{SN-lasso}(b=3K)$$
 
$$\mathrm{SN-lasso}(b=1K\&3K) \qquad \mathrm{SN-lasso}(b=1K\&3K)$$
 
$$\mathrm{NARM}(b=1K\&3K) \qquad \mathrm{NARM}(b=1K\&3K)$$

Figure S.8: **3D ROI simulation** (b = 1K, 3K, 1K&3K): FOD estimates on z-slice 4.

$$\epsilon=10^{-3} \qquad \qquad \epsilon=5\times 10^{-3}$$
 
$$\mathrm{SN-lasso}(b=1K) \qquad \mathrm{SN-lasso}(b=1K)$$
 
$$\mathrm{SN-lasso}(b=3K) \qquad \mathrm{SN-lasso}(b=3K)$$
 
$$\mathrm{SN-lasso}(b=1K\&3K) \qquad \mathrm{SN-lasso}(b=1K\&3K)$$
 
$$\mathrm{NARM}(b=1K\&3K) \qquad \mathrm{NARM}(b=1K\&3K)$$

Figure S.9: **3D ROI simulation** (b = 1K, 3K or 1K&3K): Tracking results.

$$\epsilon = 10^{-3} \qquad \qquad \epsilon = 5 \times 10^{-3}$$
 
$$\mathrm{SN-lasso}(b=1K) \qquad \qquad \mathrm{SN-lasso}(b=1K)$$
 (fiber number: 392, fiber length: 4.11) (fiber number: 3, fiber length: 0.23) 
$$\mathrm{SN-lasso}(b=3K) \qquad \qquad \mathrm{SN-lasso}(b=3K)$$
 (fiber number: 430, fiber length: 4.68) 
$$\mathrm{SN-lasso}(b=1K\&3K) \qquad \qquad \mathrm{SN-lasso}(b=1K\&3K)$$
 (fiber number: 429, fiber length: 5.03) (fiber number: 430, fiber length: 5.01) 
$$\mathrm{NARM}(b=1K\&3K) \qquad \qquad \mathrm{NARM}(b=1K\&3K)$$
 (fiber number: 435, fiber length: 5.13)

Table S.6: **3D ROI simulation** (b = 1K, 3K or 1K&3K): Success rate and angular error.

		0-Fiber	1-Fiber		2-Fiber	
$\epsilon$	Estimator	Co./Ov.	Co./Ov./Un.	Err.	Co./Ov./Un.	Err.
	SN-lasso(noiseless)	1.00/0.00	1.00/0.00/0.00	1.61	1.00/0.00/0.00	1.77
	${\tt SN-lasso}(b=1K)$	0.94/0.06	1.00/0.00/0.00	2.47	0.84/0.15/0.01	6.75
$10^{-3}$	${\tt SN-lasso}(b=3K)$	0.13/0.87	1.00/0.00/0.00	1.96	0.94/0.06/0.00	3.36
	$\verb SN-lasso (b=1K\&3K)$	1.00/0.00	1.00/0.00/0.00	1.71	0.99/0.01/0.00	2.93
	$\mathtt{NARM}(b=1K\&3K)$	1.00/0.00	1.00/0.00/0.00	1.71	1.00/0.00/0.00	2.40
	${\tt SN-lasso}(b=1K)$	1.00/0.00	0.49/0.00/0.51	2.35	0.00/0.00/1.00	-
$5 \times 10^{-3}$	${\tt SN-lasso}(b=3K)$	0.92/0.08	1.00/0.00/0.00	1.96	0.94/0.06/0.00	3.35
	$\boxed{ \texttt{SN-lasso}(b=1K\&3K) }$	1.00/0.00	1.00/0.00/0.00	1.71	0.99/0.01/0.00	2.93
	$\mathtt{NARM}(b=1K\&3K)$	1.00/0.00	0.98/0.02/0.00	1.85	1.00/0.00/0.00	2.32

Table S.7: **3D ROI simulation** (b = 1K, 3K or 1K&3K): Hellinger distance.

		True F	ODs	Noiseless estimates		
$\epsilon$	Estimator	Mean H-dist.	SD H-dist.	Mean H-dist.	SD H-dist.	
	SN-lasso(noiseless)	0.379	0.135	-	-	
	${\tt SN-lasso}(b=1K)$	0.450	0.165	0.234	0.171	
$10^{-3}$	${\tt SN-lasso}(b=3K)$	0.453	0.094	0.217	0.161	
	$\verb SN-lasso (b=1K\&3K)$	0.390	0.138	0.127	0.081	
	$\mathtt{NARM}(b=1K\&3K)$	0.381	0.135	0.105	0.062	
	${\tt SN-lasso}(b=1K)$	0.583	0.315	0.549	0.196	
$5 \times 10^{-3}$	${\tt SN-lasso}(b=3K)$	0.398	0.137	0.160	0.102	
	$\boxed{ \texttt{SN-lasso}(b=1K\&3K) }$	0.389	0.138	0.130	0.081	
	$\mathtt{NARM}(b=1K\&3K)$	0.382	0.136	0.114	0.074	

## S.2 Real D-MRI data experiments: additional details

#### S.2.1 Single tensor model

The single tensor model (Le Bihan & Warach 1995, Basser & Jones 2002, Mori 2007) for the diffusion weighted signal  $S(\boldsymbol{u})$  along the gradient direction  $\boldsymbol{u}$  is

$$S(\boldsymbol{u}) = S_0 \exp(-b\boldsymbol{u}^T \boldsymbol{D} \boldsymbol{u}),$$

where  $\mathbf{D}$  is a 3 × 3 positive definite matrix, known as the diffusion tensor. Let  $\lambda_1$ ,  $\lambda_2$  and  $\lambda_3$  be three eigenvalues of  $\mathbf{D}$ , the fractional anisotropy (FA) and the mean diffusivity (MD) are then defined as:

$$FA = \frac{\sqrt{(\lambda_1 - \lambda_2)^2 + (\lambda_2 - \lambda_3)^2 + (\lambda_3 - \lambda_1)^2}}{\sqrt{2(\lambda_2^2 + \lambda_2^2 + \lambda_3^2)}}, \quad MD = \frac{\lambda_1 + \lambda_2 + \lambda_3}{3}.$$

 $FA \in [0, 1]$  can be regarded as the indicator of diffusion pattern, where large FA indicates anisotropic diffusion along the principle eigenvector of  $\mathbf{D}$ , and small FA indicates isotropic diffusion (if the single tensor model holds). On the other hand, MD describes the diffusion rate, where large MD indicates fast diffusion and small MD indicates slow diffusion.

## S.2.2 Real D-MRI data experiments – HCP: additional details

Figure S.10: **ROI I in HCP**: (a) From left to right: Fiber orientation colormap at z-slice 71 (ROI is indicated by white box), fiber orientation colormap, FA map and MD map on ROI at z-slice 71. (b) FOD estimates on ROI at z-slice 71 (FA map is drawn on the background and the size of the FOD estimate is modulated by MD).

(a) Fiber orientation colormap, FA map and MD map

Colormap of z-slice 71 Colormap of ROI FA map of ROI MD map of ROI

(b) FOD estimates for ROI on z-slice 71

$$\mathtt{SN-lasso}(\mathtt{voxel-wise})(b=1K)$$
  $\mathtt{SN-lasso}(\mathtt{voxel-wise})(b=3K)$ 

$${\tt SN-lasso(voxel-wise)}(b=1K\&2K\&3K) \qquad \qquad {\tt NARM}(b=1K\&2K\&3K)$$

Figure S.11: **ROI I in HCP**: FOD estimates on a  $6 \times 6$  subregion at z-slice 71.

$${\tt SN-lasso(voxel-wise)}(b=1K) \qquad {\tt SN-lasso(voxel-wise)}(b=3K) \\ {\tt SN-lasso(voxel-wise)}(b=1K\&2K\&3K) \qquad {\tt NARM}(b=1K\&2K\&3K)$$

Figure S.12: **ROI I in HCP**: Tracking results.

(a) 
$$SN-lasso(voxel-wise)(b=1K)$$
 (b)  $SN-lasso(voxel-wise)(b=3K)$  (fiber number: 3556, fiber length: 4.30) (fiber number: 5445, fiber length: 5.32) (c)  $SN-lasso(voxel-wise)(b=1K\&2K\&3K)$  (d)  $NARM(b=1K\&2K\&3K)$  (fiber number: 4596, fiber length: 5.84) (fiber number: 5007, fiber length: 6.80)

Figure S.13: **ROI II in HCP**: (a) From left to right: Fiber orientation colormap at z-slice 82 (ROI is indicated by white box), fiber orientation colormap, FA map and MD map on ROI at z-slice 82. (b) FOD estimates on ROI at z-slice 82.

(a) Fiber orientation colormap, FA map and MD map Colormap of z-slice 82 Colormap of ROI FA map of ROI MD map of ROI (b) FOD estimates for ROI on z-slice 82  ${\tt SN-lasso(voxel-wise)}(b=1K) {\tt SN-lasso(voxel-wise)}(b=3K)$ 

NARM(b = 1K&2K&3K)

SN-lasso(voxel-wise)(b = 1K&2K&3K)

Figure S.14: ROI II in HCP: FOD estimates on a  $5 \times 5$  subregion at z-slice 82.

$$\begin{aligned} & \text{SN-lasso}(\text{voxel-wise})(b=1K) & \text{SN-lasso}(\text{voxel-wise})(b=3K) \\ & \text{SN-lasso}(\text{voxel-wise})(b=1K\&2K\&3K) & \text{NARM}(b=1K\&2K\&3K) \end{aligned}$$

Figure S.15: ROI II in HCP: Tracking results.

(a) SN-lasso(voxel-wise)(b = 1K) (b) SN-lasso(voxel-wise)(b = 3K)

(fiber number: 7933, fiber length: 4.21) (fiber number: 12249, fiber length: 6.13)

(c) SN-lasso(voxel-wise)(b = 1K&2K&3K) (d) NARM(b = 1K&2K&3K)

(fiber number: 9374, fiber length: 6.43) (fiber number: 9075, fiber length: 7.65)